

1 **Chemical and structural control of the partitioning of**
2 **Co, Ce, and Pb in marine ferromanganese oxides**

3
4
5 Yoshio Takahashi,^{1,2*} Alain Manceau³,
6 Nicolas Geoffroy³, Matthew A. Marcus,⁴ and Akira Usui⁵

7
8
9 ¹Department of Earth and Planetary Systems Sci., Graduate School of Sci.,
10 Hiroshima University, Higashi-Hiroshima, Hiroshima 739-8526, Japan

11 ²Laboratory for Multiple Isotope Research for Astro- and Geochemical Evolution (MIRAGE),
12 Hiroshima University, Hiroshima 739-8526, Japan

13 ³Environmental Geochemistry Group, LGIT, Univ. J. Fourier and CNRS, BP 53, 38041
14 Grenoble Cedex 9, France

15 ⁴Advanced Light Source, Lawrence Berkeley National Laboratory, One Cyclotron Road,
16 Berkeley, CA 94720, USA

17 ⁵Department of Natural Environmental Science, Faculty of Science, Kochi University, Kochi-shi,
18 Kochi 780-8520, Japan

19
20 Corresponding author: ytakaha@hiroshima-u.ac.jp

21 Running Head: Co, Ce and Pb in marine ferromanganese oxides

22 Index terms: XANES, EXAFS, Co, Ce, Pb, ferromanganese oxide, vernadite, ferrihydrite,
23 oceanic nodule,

ABSTRACT

24
25
26 The oxidation state and mineral phase association of Co, Ce and Pb in hydrogenetic,
27 diagenetic, and hydrothermal marine ferromanganese oxides were characterized by X-ray
28 absorption near-edge structure (XANES) and extended X-ray absorption fine structure (EXAFS)
29 spectroscopy and chemical extraction. Cobalt is trivalent and associated exclusively with the Mn
30 oxide component (vernadite). Cerium is tetravalent in all genetic-type oxides (detection limit for
31 Ce(III) ~ 5 at. %), including Fe-rich areas (ferrihydrite) of hydrogenetic oxides, and is associated
32 primarily with vernadite. Thus, the extent of a Ce anomaly does not result from variations in
33 redox conditions, but appears to be kinetically controlled, decreasing when the growth rate
34 increases from hydrogenetic to diagenetic to hydrothermal oxides. Lead is divalent and
35 associated with Mn and Fe oxides in variable proportions. According to EXAFS data, Pb is
36 mostly sorbed on edge sites at chain terminations in Fe oxide and at layer edges in Mn oxide (ES
37 complex), and also on interlayer vacancy sites in Mn oxide (TCS complex). Selective dissolution,
38 spectroscopic data, and electrochemical considerations suggest that the geochemical partitioning
39 in favor of the Mn oxide component decreases from Co to Ce to Pb, and depends on their
40 oxidative scavenging by Mn and Fe oxides.

41

1. INTRODUCTION

42
43
44 Marine ferromanganese oxides are found in a variety of environments and forms, such as
45 hydrogenetic nodules and crusts on the deep-sea floor, diagenetic precipitates in sediments,
46 hydrothermal deposits near oceanic ridges, and sinking Fe-Mn colloidal particles in the water
47 column (Glasby, 2000). A common trait to all ferromanganese oxides is their enrichment in trace
48 elements relative to seawater. Their ubiquity, abundance, and importance in the cycling of trace
49 elements has aroused the interest of scientists for several decades, in particular with respect to the
50 geochemical partitioning and incorporation mechanisms of trace elements. These questions often
51 have been addressed by interelement correlations using bulk chemical analysis (e.g., Moorby and
52 Cronan, 1981; Calvert and Piper, 1984; Aplin and Cronan, 1985a,b; De Carlo and McMurtry,
53 1992; Wen et al., 1997), and selective dissolution (Moorby and Cronan, 1981; Aplin and Cronan,
54 1985b; Koschinsky and Halbach, 1995; Koschinsky and Hein, 2003). Few studies have used
55 non-invasive spectroscopic methods, although they offer direct, and often unique, access to the
56 problem (e.g., Dillard et al., 1982; Takahashi et al., 2000; Kuhn et al., 2003; Marcus et al.,
57 2004a).

58 In this paper, the oxidation states of Co, Ce, and Pb in hydrogenetic, diagenetic, and
59 hydrothermal ferromanganese oxides were determined by X-ray absorption near-edge structure
60 (XANES) spectroscopy to evaluate the importance of redox reactions in trace element
61 partitioning (Goldberg, 1961, 1965; Goldberg et al., 1963; Piper, 1974; Burns, 1976). Dillard et al.
62 (1982) concluded using X-ray photoelectron spectroscopy (XPS) that cobalt is trivalent in marine
63 ferromanganese oxides, and Takahashi et al. (2000) that cerium is tetravalent using XANES
64 spectroscopy. These two studies were limited to metal-rich hydrogenetic samples. Pb enrichment
65 in ferromanganese oxides has been suggested to result from Pb(II) to Pb(IV) oxidation (Goldberg,
66 1965; Murray and Dillard, 1979), but this hypothesis has received little experimental support
67 (Dillard et al., 1981). The abundances of Co, Ce, and Pb decrease on average from hydrogenetic

68 to diagenetic to hydrothermal deposits (Usui et al., 1997), and the possibility that this evolution is
69 associated with a variation of their oxidation state has not been investigated. Such a relationship
70 would provide insight into chemical processes responsible for the enrichment of redox-sensitive
71 trace elements in ferromanganese oxides. In particular, questions remain as to the reasons for the
72 variability of the Ce anomaly in REE (rare earth elements) patterns, and its possible link to Ce
73 oxidation state.

74 When considering redox reactions in ferromanganese oxides, elemental distribution
75 among Mn and Fe oxides is an important issue. The nature of the trace element host phases were
76 investigated by electron microprobe, micro-XANES spectroscopy (μ -XANES), and Pb L_{III}-edge
77 extended X-ray absorption fine structure (EXAFS) spectroscopy, and the results compared to
78 those from sequential dissolution to assess the usefulness of chemical extraction to speciate trace
79 metals in ferromanganese matrices.

80

81

2. MATERIALS AND METHODS

2.1. Samples

83

84 Seventeen samples collected during several research cruises in the Central to NW Pacific
85 Ocean and the Central Indian Ocean were selected for this study (Table 1). They were classified
86 into hydrogenetic (HG), diagenetic (DG), and hydrothermal (HT) origins on the basis of the
87 mineralogy of the Mn oxide, as summarized in Table 1 (Takematsu, 1998). Samples 31GTV2-3
88 and 31GTV6-11 have a mixed hydrogenetic and hydrothermal origin (Kuhn et al., 1998). The
89 two samples had fast growth rates (10-20 mm/Myr) due to the supply of Mn and Fe from
90 hydrothermal plumes, but their trace elements are considered to be derived mainly from seawater.
91 Thus, they are labeled HT + HG in Table 1. Nodule D465 has a hydrogenetic core and a
92 diagenetic rim and the two parts were analyzed separately. Samples containing P-rich layers were
93 disregarded because secondary phosphatization may modify the original distribution of trace

94 elements (Koschinsky et al., 1997). According to this reference, P concentration in phosphatized
95 crusts is higher than 2.5 wt. %, a value well above the P content of our samples (see Results
96 section).

97

98 **2.2. Reference materials**

99

100 CoO (purity > 99.9 %), orthorhombic PbO (> 99.9 %), Pb₃O₄ (> 99 %), PbO₂ (> 99.9 %),
101 CeCl₃ (> 99 %), Ce(SO₄)₂ (> 99.5 %), and CeO₂ (> 99.9 %) from Wako Pure Chemical
102 Industries, Ltd., Katayama Chemicals, and Rare Metallic Co., Ltd. were used as references for
103 XANES measurements. Powders were diluted to 0.5 wt. % in boron nitride and pressed into
104 pellets. A Ce(OH)₄ gel was prepared by hydrolyzing a Ce(NH₄)₂(NO₃)₆ solution at pH 7 in
105 contact with air (Sumaoka et al., 2000). No Ce(IV) reduction occurs at this Eh-pH condition
106 (Brookins, 1988). The Ce(OH)₄ gel recovered by filtration was re-suspended in water at pH ~7
107 and adjusted to a 0.5 wt. % Ce concentration for XANES analysis.

108 Ferrihydrite (HFO) and δ -MnO₂ used in Co, Ce, and Pb sorption experiments for XANES
109 measurements were synthesized according to Schwertmann and Cornell (2000) and Murray
110 (1974), respectively. Sorption samples were prepared by adding 10 mL of 17.0 μ M Co(II), 7.15
111 μ M Ce(III), or 4.83 μ M Pb(II) solutions (pH 5) prepared from nitrate salts to 1 mg ferrihydrite or
112 δ -MnO₂ in suspension in synthetic seawater (Nishimura, 1983) at equilibrium with air. Final pH
113 was adjusted to 7.0 (Co), 6.6 (Ce) and 6.5 (Pb) by incremental addition of HCl. The final pH was
114 lower than that of seawater (8.2 ± 0.1) to prevent metal precipitation. The solid phases were
115 recovered by filtration (0.45 μ m; hydrophilic PTFE) after 1 hour of reaction time, washed with
116 bidistilled water (Milli-Q), and packed wet into polyethylene bags for XANES measurements. A
117 Ce-sorbed ferrihydrite sample was equilibrated for 120 hours. The Ce, Co and Pb concentrations
118 in the solid phases are about 0.1 wt. %.

119 A separate series of Pb-sorbed δ -MnO₂ samples were prepared as follows for EXAFS

120 measurements. δ -MnO₂ was prepared by reducing at pH 7 a KMnO₄ solution with MnCl₂
121 (Villalobos et al., 2005). The precipitate was washed, dialyzed, and stored at 5°C in
122 polypropylene containers for several days at the synthesized solid concentration (21.7 g/L).
123 Pb-sorption samples were prepared by addition of a Pb(NO₃)₂ solution to a δ -MnO₂ suspension
124 (2 g/L, 0.1 M NaNO₃) that had been pre-equilibrated at the desired pH with an automatic titrator.
125 After allowing several hours for equilibration at constant pH, the sorption sample was filtered on
126 a 0.1 μ m cellulose nitrate membrane, washed with Milli-Q water to prevent the precipitation of
127 metal salt, and freeze-dried. We know from previous studies, and from the similarity of our
128 Pb-EXAFS data (see Results section) with those collected on wet pastes (Villalobos et al., 2005)
129 and powders frozen to 10-20 K (Morin et al., 2001), that the binding mechanism of hydrolyzable
130 cations on phyllo-manganates is not modified by freeze-drying, probably because they form
131 multidentate inner-sphere complexes (Lanson et al., 2002a; Manceau et al., 2002a). Also, the
132 stability in vacuum of the layer of water in the interlayer of δ -MnO₂ and birnessite, which is
133 attested by the persistence of the basal X-ray reflection at ~ 7 Å, supports the view that data
134 collected on freeze-dried samples are representative of surface complexes at the water-mineral
135 interface. Four samples were prepared at pH 5 and Pb/Mn molar ratios, as measured by
136 inductively coupled plasma-atomic emission spectrometry (ICP-AES), of 0.002 (PbdBi2), 0.044
137 (PbdBi44), 0.112 (PbdBi112), and 0.197 (PbdBi197). One sample was prepared at pH 7 and
138 intermediate surface loading to test the influence of pH on the structure of the Pb surface
139 complex on δ -MnO₂. Its EXAFS spectrum was almost identical to the PbdBi44 spectrum (data
140 not shown). The effect of crystallinity was investigated by comparing the data with those for Pb
141 sorbed on well-crystalline hexagonal birnessite at pH 4 and Pb/Mn molar ratio of 0.031 (sample
142 PbBi31 in Lanson et al., 2002a). This reference had been characterized by EXAFS spectroscopy
143 previously (Manceau et al., 2002a), but a higher quality spectrum was recorded for this study.

144

145 **2.3. Chemical compositions**

146
147 The Mn, Fe, Co, Ni, Cu, and Zn concentrations in the natural samples were measured by
148 ICP-AES (Yanaco UOP-1S) after acid digestion using HF/HCl/HNO₃, and Pb concentration was
149 measured by inductively coupled plasma-mass spectrometry (ICP-MS) (VG PQ-3) using Bi as an
150 internal standard. The precision and accuracy of the analytical values were better than 10 %,
151 based on the analysis of the JMn-1 reference prepared from ferromanganese oxide deposits
152 distributed by the Geological Survey of Japan (GSJ; Terashima et al., 1995). REE abundances
153 were measured by ICP-MS using In and Bi as internal standards (Takahashi et al., 2000).
154 Repeated analyses on JB-1a standard rock prepared by GSJ showed that the precision and
155 accuracy of the REE analyses were generally better than 5 %. REE abundances for D513 are
156 from Ohta et al. (1999), and major and minor (including REE) element concentrations for
157 31GTV2-3 and 31GTV6-11 are from Kuhn et al. (1998). Major elements and Co, Ni, Cu, Zn, Ce,
158 and Pb concentrations in samples CD25, D535, AD14, D465, D514, and FG352 were measured
159 also with an electron probe microanalyzer (EPMA, JXA-8200, JEOL), running at 15 keV
160 acceleration voltage and using a 5 μm-sized beam.

161

162 **2.4. Sequential leaching experiments**

163

164 Sequential leaching experiments were performed on powdered samples, following the
165 procedure described in Koschinsky and Hein (2003) and Koschinsky and Halbach (1995). Briefly,
166 0.5 g of powder was mixed with 15 mL of 1 M acetic acid/Na acetate buffer (pH 5) at room
167 temperature for 5 hours. The filtrate (fraction 1) was considered to include exchangeable cations
168 and cations initially present in carbonates. The residue was suspended in 25 mL of Milli-Q water
169 and stirred with 87.5 mL of a 0.1 M hydroxylamine hydrochloride (NH₃OHCl) solution (pH 2)
170 for 24 hours. The filtrate at this step (fraction 2) contained cations originally in Mn oxides. The
171 new residue was suspended in 100 mL of Milli-Q water and stirred with 87.5 mL of 0.2 M oxalic

172 acid/ammonium oxalate buffer (pH 3.5) for 12 hours. The filtrate (fraction 3) contained cations
173 originally associated with Fe oxides. The final residue, mainly consisting of silicates and
174 aluminosilicates (fraction 4), was digested for bulk chemical analyses. The Mn, Co, Pb, and Ce
175 concentrations in all filtrates were measured by ICP-MS after dilution by a factor > 100 in 2 %
176 HNO₃, and the Fe concentrations were measured by ICP-AES. For each element, the sum of
177 concentrations from fractions 1 to 4 divided by the bulk concentrations (i.e., recovery of the
178 leaching experiments) was better than 82 %.

179 Re-adsorption of dissolved ions on residual solid phases may occur during sequential
180 leaching experiments (Rendell et al., 1980; Sholkovitz, 1989; Gilmore et al., 2001). The fractions
181 of metals re-adsorbed on Fe oxides and insoluble phases (silicate and aluminosilicates) in the
182 hydroxylamine hydrochloride extraction step were determined using ⁵⁴Mn, ⁵⁸Co, ¹³⁹Ce, and ¹⁴⁶Gd
183 radioisotope tracers (Ambe et al., 1995; Takahashi et al., 1997; Takahashi et al., 1999). Lead
184 radioisotopes were not included in the multitracer solution, and thus Pb was not analyzed. The
185 amounts of re-adsorbed radioisotopes were obtained by measuring the γ -ray spectrum of the
186 filtrate with a Ge solid-state detector. Counting was stopped when the total number of counts was
187 at least 10,000 for each radioisotope. Measurements of the peak area and corrections of the decay
188 of each isotope were carried out by a routine procedure.

189

190 **2.5. XANES and EXAFS measurements and analyses**

191

192 Cerium L_{III}-edge and Co K-edge XANES spectra were recorded on beamline BL12C at the
193 KEK Photon Factory in Tsukuba, Japan (Nomura and Koyama, 1996), and Pb-L_{III}-edge XANES
194 spectra on beamline BL01B1 at SPring-8 in Hyogo, Japan (Uruga et al., 1999). The two
195 beamlines have similar layouts. The X-rays were monochromatized with a pair of Si(111)
196 crystals. The beam size at the sample position was about $1 \times 1 \text{ mm}^2$, and its intensity (I_0)
197 monitored with an ionization chamber. The sample was placed at 45 degrees from the incident

198 beam, and the fluorescent X-rays measured with a 19 element Ge solid-state detector. At the Co
199 K-edge, the intensity of the unwanted fluorescence signal from Mn and Fe was reduced by
200 mounting a vanadium filter ($\mu t = 3$ or 6) in front of the detector. Deadtime correction was done
201 by the method of Nomura (1998). Energy was calibrated by assigning the energy of the first peak
202 of CeO_2 at 5730.5 eV (Ce L_{III} -edge), the absorption maximum of CoO (Co K-edge) at 7730.3 eV,
203 and the absorption maximum of PbO_2 (Pb L_{III} -edge) at 13061.5 eV (the first maximum of the
204 derivative of elemental Pb was at 13029 eV). XANES spectra were recorded with a 0.25 to 1 eV
205 step size and 1 to 5 sec counting per step. One to five scans were summed to improve the
206 signal-to-noise ratio, and all spectra were normalized to unit step in the absorption coefficient. No
207 radiation damage was detected during the data acquisition.

208 Bulk XANES measurements were complemented by micro-XANES and X-ray fluorescence
209 (XRF) mapping measurements for the hydrogenetic ferromanganese nodule CD25. The
210 experiments were carried out on beamline 10.3.2 at the Advanced Light Source (ALS), Lawrence
211 Berkeley National Laboratory, USA (Manceau et al., 2002b; Marcus et al., 2004b). The sample
212 was embedded in a high purity resin (Eposet, Maruto Co.,Ltd.), polished on one face, and glued
213 on a glass slide with a wax product (Skywax 415, Maruto Co., Ltd.). After polishing the other
214 face of the sample to a thickness of about 30 μm , the thin section was removed from the glass
215 support by dissolving the wax in *o*-xylene. An area of $1.2 \times 1.1 \text{ mm}^2$ from the free-standing
216 specimen was scanned under a $5 \times 5 \mu\text{m}^2$ beam using steps of 5 μm . The distribution of Co and
217 Ce were imaged by recording, for each element, one map above and another below their
218 absorption K edges (7659 and 7759 eV for Co; 5718 and 5730.5 eV for Ce, respectively) and
219 calculating the difference maps. From visual comparison of these elemental distributions, and
220 from the Mn/Fe ratio, specific points-of-interest (POIs) were selected for Co K-edge and Ce
221 L_{III} -edge micro XANES measurements. To avoid the possibility of radiation damage, only one
222 spectrum was collected at each spot, and spectra from nearby spots having similar compositions
223 as seen from the XRF maps were averaged.

224 Fluorescence-yield Pb-EXAFS spectra of the two hydrogenetic samples D1-X1 and D21-m3
225 before treatment and after dissolution of the Mn oxides, as described in section 2.4, were
226 recorded on the FAME (BM 30B) beamline at the European synchrotron radiation facility
227 (ESRF) in Grenoble, France. The white X-ray beam was collimated vertically to 3 mm with a
228 bent Rh-coated Si mirror, monochromatized with a two-crystal Si (220) monochromator, sagittally
229 focused to 300 μm with the second crystal, and vertically focused to 150 μm with a second bent
230 Rh-coated Si mirror downstream of the monochromator (Hazemann et al., 1995; Proux et al.,
231 2006). X-ray fluorescence was detected with a 30-Ge solid-state detector, and the output signal
232 processed with a fast amplifier (0.125 μs shaping time, 300 eV FWHM resolution). Multiple
233 scans were performed to improve statistics. To avoid the possibility of radiation damage, the
234 sample pellet was moved by 0.5 mm after each scan.

235 The EXAFS data analysis was carried out using the codes from the WinXAS package
236 (Ressler, 1998). Phase shifts and amplitude functions for the simulation of data were calculated
237 by FEFF7 (Ankudinov and Rehr, 1997) with quenselite as a structural model (Rouse, 1971). The
238 experimental EXAFS function, $\chi(k)$, was obtained after subtracting the embedded-atom
239 absorption background from the Pb-L α fluorescence signal normalized to the intensity of the
240 incident beam (I_0), and normalizing the signal by the edge step. EXAFS spectra were Fourier
241 transformed with a Bessel apodization function to real (R) space, and backtransformed to k space
242 for spectral simulation.

243

244

3. RESULTS

245

3.1. Chemical composition

247

248 Abundances of Mn, Fe, Co, Ni, Cu, Zn, and Pb in bulk samples and in the local areas
249 measured by EPMA are listed in Tables 2 and 3. The contents of Co and Pb against the Mn/Fe

250 ratio are plotted in Figure 1. We know from previous studies (e.g., Moorby and Cronan, 1981;
251 Calvert and Piper, 1984; Aplin and Cronan, 1985a,b; De Carlo and McMurtry, 1992; Usui et al.,
252 1997 Wen et al., 1997) that the Mn/Fe ratio increases, and Co and Pb concentrations generally
253 decrease, from hydrogenetic to diagenetic to hydrothermal Mn formations. Aside from samples
254 31GTV2-3 and 31GTV6-11, our data are consistent with this general trend, which confirms that
255 the series of samples includes the three genetic types of ferromanganese oxide. The singularity of
256 the two GTV samples, classified as a mixture of hydrogenetic and hydrothermal oxides, is
257 explained by the incorporation of trace elements from seawater (hydrogenetic characteristic) at a
258 fast growth rate (hydrothermal characteristic) (Kuhn et al., 1998).

259 REE abundances are listed in Table 4, and values normalized to those of the Post-Archean
260 Australian Shale, PAAS (McLennan, 1989) are plotted in Fig. 2a. REE are abundant in
261 hydrogenetic oxides, intermediate in diagenetic oxides, and low in hydrothermal oxides. The Ce
262 anomaly $(\text{Ce}/\text{Ce}^*)_{\text{SN}}$ reported in Table 4 was calculated by defining $(\text{Ce}^*)_{\text{SN}} = (\text{La}^{1/2}\text{Pr}^{1/2})_{\text{SN}}$
263 (Akagi and Masuda, 1998), where the subscript SN denotes the abundance normalized to PAAS.
264 The Ce anomaly is referred to as positive ($[\text{Ce}/\text{Ce}^*]_{\text{SN}} > 1$) in hydrogenetic and negative
265 ($[\text{Ce}/\text{Ce}^*]_{\text{SN}} < 1$) in hydrothermal oxides. Diagenetic samples have intermediate values that are
266 close to 1. The decrease in REE abundance and inversion of the Ce anomaly along the
267 hydrogenetic - diagenetic - hydrothermal series is consistent with previous studies (e.g., Usui et
268 al., 1997), confirming that the series of samples is representative of the three genetic types of
269 marine ferromanganese oxide.

270

271 **3.2. Sequential dissolution**

272

273 The correlation of Co, Ce and Pb with Fe, and their anti-correlation with Mn in Figure 1 do
274 not necessarily imply that they are chemically bound to or included in the structure of the Fe
275 oxide component (ferrihydrite). To gain further insight, sequential dissolution experiments were

276 conducted on four hydrogenetic samples (D535, AD14, D1-X1, and D21-m3) and two diagenetic
277 samples (FG352 and G181). The extent of Mn, Co, Ce, and Gd re-adsorption on the Fe oxide
278 after dissolution of the Mn oxide component was evaluated with the multitracer technique on
279 D535 and AD14. Mn and Co were marginally re-adsorbed ($< 3\%$), but Ce ($35 \pm 24\%$) and Gd
280 ($46 \pm 21\%$) were substantially re-adsorbed.

281 From 59% (G181) up to 97% (D535 and D1-X1) of total Co, and from 71% (G181) up to
282 95% (AD14 and D21-m3) of total Mn were leached in fraction 2 (hydroxylamine hydrochloride
283 treatment, Fig. 3), while the ratio of dissolved Fe to total Fe remained low (7% to 24%). Thus,
284 Mn oxides were preferentially dissolved over Fe oxides during the second extraction step, and
285 this chemical treatment also released most of Co. The Co-Mn association, confirmed below by
286 EPMA and XANES spectroscopy, indicates that the positive Co-Fe/Mn correlation in Figure 1 is
287 misleading about the nature of the Co host phase. From 75% (D535) to 99% (D21-m3) of total
288 Pb was leached out with Fe in fraction 3 (oxalate treatment). The co-extraction of Pb and Fe in
289 ferromanganese oxides has been interpreted as indicating Pb uptake on Fe oxides (e.g.,
290 Koschinsky and Halbach, 1995; 2003). This interpretation should be viewed cautiously, however,
291 because Pb is prone to re-adsorption (Gilmore et al., 2001), and this side-effect is expected to be
292 larger than for REE, such as Ce and Gd (Sholkovitz, 1989). Cerium extraction data are
293 conclusive for D535 and D1-X1 because Ce and Mn were eluviated together: 75% Ce and 89%
294 Mn in D535, 62% Ce and 87% Mn in D1-X1. In the other samples, Ce was eluviated
295 predominantly with Fe. Thus, re-adsorption of Mn oxide-bound Ce on Fe oxides may artificially
296 enhance the proportion of Ce initially held by the Fe phase. Therefore, Ce is at least partly
297 associated with Mn, and perhaps also with Fe.

298

299 **3.3. Electron microprobe**

300

301 The micrometer-scale variability of the Co, Ce, and Pb correlations with Fe and Mn was

302 examined by analyzing with EPMA the main growth structures of three hydrogenetic samples
303 (CD25, D535, and AD14). Fair to strong correlations were measured between Co and the Mn to
304 Fe ratio: $r^2 = 0.64$ for CD25, $r^2 = 0.76$ for D535, and $r^2 = 0.80$ for AD14 (Fig. 4). In contrast, Pb
305 and Ce lacked clear correlation with Fe and Mn.

306

307 **3.4. Cerium L_{III}-edge XANES**

308

309 The excitation energy of an element increases with its oxidation state, due to an increase in
310 binding energy of core electrons and the destabilization of antibonding states as the formal
311 valency of the metal ion increases (Bianconi, 1988). The chemical shift at the Ce L_{III}-edge is
312 illustrated in Figure 5 with CeCl₃ as Ce(III) reference, and CeO₂, Ce(OH)₄ gel, and Ce(SO₄)₂ as
313 Ce(IV) references. The trivalent species has an absorption maximum at 5726.5 eV attributed to a
314 single electronic excitation from the 2p_{3/2} to the 5d states. The tetravalent species have two
315 maxima at 5730 and 5738 eV attributed to a double electronic excitation in the final states, owing
316 to a strong hybridization of the 4f states of Ce and the ligand orbitals (Jo and Kotani, 1985;
317 Kotani et al., 1987; Soldatov et al., 1994). The absorbance of CeO₂ and Ce(OH)₄ is higher at
318 5730 eV than at 5738 eV, and the two spectra have a shoulder at about 5727 eV. These two
319 features are attributed to many-body effects and to the covalent nature of the Ce-O-Ce bond
320 (Kaindl et al., 1988; Hu et al., 1994; Soldatov et al., 1994; Takahashi et al., 2002a). They are not
321 observed in Ce(SO₄)₂ and Ce-sorbed δ -MnO₂ because of the more ionic character of the
322 Ce(IV)-O bond in these compounds (Takahashi et al., 2002a). Apart from D465 (outer), all the
323 sample spectra are similar to those of Ce(SO₄)₂ and Ce-sorbed δ -MnO₂, which indicates that Ce
324 is exclusively tetravalent in all genetic-types of ferromanganese oxide. The maximum amount of
325 Ce(III), as estimated from spectral combinations of CeCl₃ and Ce(SO₄)₂, is 5% for all samples
326 except for D465 (outer).

327 The previous set of bulk XANES spectra was complemented by a micro-XANES spectrum

328 at a Mn-rich spot (spot 1) and an Fe-rich spot (spot 2) of CD25 (Fig. 6). Spot 1 is within the main
329 growth structure, and spot 2 is in the Fe-rich region on the rim of the main growth structure.
330 From the relative intensities of the Mn K_{α} and Fe K_{β} signals, the Mn/Fe ratio at spot 1 is about
331 5.6 times higher than that at spot 2. EPMA analysis of spot 2 gave 31 wt. % Fe, 16 wt. % Si, and
332 0.32 wt % Mn. The Fe-Si association may be due to nontronite (Sorem and Fewkes, 1977;
333 Halbach et al., 1988; Takematsu, 1998). Si may be speciated also as amorphous silica (opal).
334 Regardless of the contrasted chemical composition of the two analyzed spots, their XANES
335 spectra were similar and indicative of Ce(IV) only.

336 The nature of the main Ce host phase can be inferred from data on the two sorption
337 references. Figure 5 shows that Ce(III) was oxidized completely to Ce(IV) on δ -MnO₂, but not
338 on ferrihydrite (HFO). The small absorption feature at 5738 eV in the HFO spectra is suggestive
339 of Ce(IV), but this species clearly is minor. Therefore, since Ce is tetravalent in all samples, it
340 should be associated primarily with the Mn oxide component and not, or in subordinate amounts,
341 with the Fe oxide component. This interpretation supposes that ferrihydrite does not oxidize Ce
342 in the physico-chemical conditions of the marine environment, which may not be correct.
343 According to Bau (1999), the ferric oxide reference would have contained more Ce(IV) if
344 sorption had been performed on freshly precipitated colloidal particles rather than on a preformed
345 solid.

346

347 **3.5. Cobalt K-edge XANES**

348

349 Figure 7 shows the Co K-edge XANES spectra of a selection of samples together with those
350 of CoO and Co₂O₃, as references for Co(II) and Co(III), respectively. The chemical shift of the
351 absorption maxima for octahedral Co(II) (7730 eV) and Co(III) (7734 eV) is 4 eV, and can be
352 used to determine the oxidation state of Co in unknown samples (Manceau et al., 1987, 1992a).
353 The sample spectra match the δ -MnO₂ reference, and their edge energy is characteristic of

354 trivalent Co. Two micro-XANES spectra were measured at spots 1 and 2 of CD25 (Fig. 8). From
355 the Co K α data, the Co concentration is 3.3 times higher at spot 1 than at spot 2. The two point
356 XANES spectra are essentially the same and typical of Co(III). However, a weak shoulder at the
357 energy of the maximum absorbance for the Co(II) species (7729 eV) is apparent on the spot 2
358 spectrum when the spot 1 spectrum is overlaid. The lineshape of the spot 2 spectrum could be
359 reproduced with a linear combination of 80-85 % spot 1 + 10-15 % CoO. This result provides
360 suggestive evidence for some Co-HFO association, but the data are too noisy to draw a definitive
361 conclusion. Therefore, we conclude that Co is trivalent in hydrogenetic (CD25, D465 inner),
362 diagenetic (G181, D465 outer), and hydrothermal (D21-103) Mn oxides. Similarly to Ce, the
363 non-oxidation of Co(II) at the ferrihydrite surface in contact with air, and its oxidation on δ -MnO₂
364 (Fig. 7), provide strong evidence for Co association to the Mn oxide component.

365

366 3.6. Lead L_{III}-edge XANES

367

368 Figure 9a shows the Pb L_{III}-edge XANES spectra of a selection of hydrogenetic (CD25,
369 D1-X1, D465 (inner), and D21-m3) and diagenetic (D465 (outer) and G181) ferromanganese
370 oxides, and the two sorption (HFO, δ -MnO₂) and the PbO, Pb₃O₄, and PbO₂ references. The
371 spectra from the natural and synthetic samples resemble the PbO spectrum. Since Pb-XANES
372 spectra are essentially featureless, first derivatives are generally plotted to enhance the spectral
373 sensitivity to the electronic structure of Pb (Rao and Wong, 1984; Bargar et al., 1997a; Choi et al.,
374 1999). The 2p to 6s electronic transition at 13.029 keV is possible for the Pb(IV) species owing to
375 its (5d)¹⁰(6s)⁰ configuration, but not for Pb(II), since the two 6s electronic levels are filled in this
376 species. The 2p \rightarrow 6s transition is absent in all spectra from natural and synthetic samples, which
377 indicates that Pb is divalent in marine ferromanganese oxides, and that no oxidation occurred
378 upon Pb sorption on HFO and δ -MnO₂, in agreement with previous experimental studies
379 (Manceau, 1992b; Bargar et al., 1998; Matocha et al., 2001; Trivedi et al., 2003; Villalobos et al.,

380 2005). As Pb is dissolved as a divalent species, such as PbCl_n^{2-n} and PbCO_3^0 , in seawater (Byrne,
381 2002), and as many redox reactions are catalyzed at mineral surfaces (Wehrli, 1990), it has been
382 conjectured that the oxidation of Pb(II) to Pb(IV) is the main enrichment mechanism of Pb in
383 marine ferromanganese oxides (Goldberg, 1965; Hem, 1978; Murray and Dillard, 1979;
384 Nishimura, 1983; Halbach et al., 1988). This hypothesis is not supported by our data.

385 Since Pb is not oxidized by Mn oxides, XANES data do not allow determining whether Pb is
386 associated with the Fe or Mn oxide component. Based on sequential extraction data, Pb is
387 associated with Fe, but this macroscopic technique for determining metal speciation has pitfalls,
388 as mentioned previously. To answer this question, the three hydrogenetic samples AD14, D1-X1
389 and D21-m3 were examined by EXAFS spectroscopy.

390

391 **3.7. Lead L_{III} -edge EXAFS**

392

393 *3.7.1. Pb mineral host*

394

395 The mineralogical nature of the Pb host in AD14, D1-X1 and D21-m3 was determined by
396 recording the EXAFS spectra of the untreated and hydroxylamine hydrochloride treated (fraction
397 2) samples. The spectra can be classified in three groups on the basis of their shape and
398 frequency: AD14, D1-X1 and D21-m3, and the three treated samples (Fig. 10a-e). The spectra
399 within each of the second and third groups are statistically invariant, as illustrated in Figure 10b
400 with D1-X1 and D21-m3. These two spectra could be reconstructed with a linear combination of
401 untreated AD14 and either of the treated samples (Fig. 10f). Consequently, the whole data set
402 forms a binary system which is bounded by AD14 and the Mn-free samples (fraction 2).
403 Comparison of the fraction 2 spectra with Pb-sorbed Fe (oxyhydr)oxides references from a
404 database showed that the treated spectra matched best the ferrihydrite spectrum (PbHFO100), Fig.
405 11a,b). This result is consistent with chemistry and diffraction data, since Fe is speciated as

406 ferrihydrite in these samples.

407 The nature of the Pb host in AD14 was determined by comparing its spectrum with those
408 from the Pb-sorbed δ -MnO₂ references. The PbBi112 spectrum provided the best match to the
409 data (Fig. 11c,d). The ferromanganese and reference spectra are similar, differing only in the
410 shape of the ascending part of the second oscillation. Qualitatively, one may conclude that Pb has
411 a similar binding environment, and hence likely occupies the same crystallographic sites, in the
412 natural and synthetic phyllomanganates. This interpretation is supported by the Fourier
413 transforms, which show that Pb has a similar local structure in the two solids. Linear
414 combinations of Mn and Fe (oxyhydrox)oxide references verified that Pb is associated only with
415 the Mn oxide phase in AD14, with a detection limit for Pb-ferrhydrite estimated at 10 %. Since
416 AD14 and the fraction 2 spectra are from pure species, the fractional amounts of Fe- and
417 Mn-bound Pb in D1-X1 and D21-m3 can be estimated from their spectral reconstruction with the
418 two single species spectra. The best fits to the D1-X1 and D21-m3 spectra were obtained with 50
419 \pm 10 % Mn-bound Pb and 47 \pm 10 % Fe-bound Pb (Fig. 10f).

420

421 3.7.2. Uptake mechanism of Pb

422

423 The nature of the polyhedral connectivity between Pb and the Fe(O,OH)₆ octahedra in
424 ferrihydrite was determined by least-squares fitting the reference rather than the sample data
425 because the former had a higher signal-to-noise ratio. The Fourier transform of PbHFO100
426 exhibits a Pb-O peak at $R + \Delta = 1.8 \text{ \AA}$ and a Pb-Fe peak at $R + \Delta = 2.9\text{-}3.0 \text{ \AA}$, or $R \sim 2.3 \text{ \AA}$ and
427 $3.3 - 3.4 \text{ \AA}$, respectively, after semi-quantitative correction of the phase-shift effect (Manceau et
428 al., 1992b; Ford et al., 1999; Scheinost et al., 2001; Trivedi et al., 2003) (Fig. 11b). More precise
429 interatomic distances were obtained from spectral fits. The best fit structural parameters derived
430 from a two-shell fit model were 2.8 O atoms at 2.36 \AA and 1.6 Fe at 3.39 \AA (Fig. 12a; Table 5).
431 This model failed to reproduce the wave node at 4.8 \AA^{-1} and the shape of the third oscillation at 7

432 \AA^{-1} . Splitting the first oxygen shells in two subshells moderately improved the simulation, but
433 splitting the iron shell improved it quite significantly as it halved the goodness-of-fit parameter
434 (Fig. 12b-d, Table 5). An optimal fit to the data was obtained with a four-shell model consisting
435 of about 3 O at 2.38 \AA , 1 O at 2.65 \AA , 2 Fe at 3.32 \AA and 2 Fe at 3.50 \AA (Fig. 12d). The Pb-O
436 distances are characteristic of divalent Pb (Manceau et al., 1996), and the Pb-Fe distances of a
437 bidentate edge-sharing complex (ES) between the Pb and Fe coordination polyhedra.

438 In contrast to ferrihydrite, the Pb-metal shell peak is a doublet (Mn1 and Mn2) in the Fourier
439 transform of AD14 (Fig. 11d), which is evidence for at least two Pb-Mn distances. Since the two
440 Pb-Mn peaks are weak, the geometry of the Pb surface complex and nature of the sorption site in
441 AD14 were determined from the analysis of the Pb sorption reference spectra. The five
442 phyllomanganate spectra intersect at the same k values, which signifies that the system is binary
443 (Manceau et al., 1998), and thus that the local structure of Pb varies continuously between two
444 well-defined configurations (Fig. 13a). On the Fourier transforms, the Mn2 peak has a high
445 amplitude and the Mn1 peak a weak amplitude at high surface loading in the δ -MnO₂ series, and
446 even more so in well-crystallized birnessite (PbBi31). Decreasing the surface loading down to
447 Pb/Mn = 0.002 (sample PbdBi2) on δ -MnO₂ increased the amplitude of the Pb-Mn1 peak and
448 concomitantly decreased that of the Pb-Mn2 peak (Fig. 13b). The dependence of the relative
449 amplitude of the two Pb-Mn peaks on the Pb/Mn ratio and crystallinity demonstrates the presence
450 of two surface complexes having a different affinity for the phyllomanganate surface, as shown
451 previously for Zn on phyllomanganate (Manceau et al., 2002a; Toner et al., 2006) and Cd on
452 goethite (Spadini et al., 1994). When the surface coverage is low and the surface area high (i.e.,
453 δ -MnO₂), the short distance Pb species prevails, meaning that it has a high affinity for the mineral
454 surface, while it is outnumbered by the long distance and lower affinity Pb species at high surface
455 coverage.

456 Good spectral agreement between theory and experiment for the δ -MnO₂ series was obtained

457 by considering only one shell of oxygens at 2.3 Å and two Mn shells (Mn1 and Mn2) at 3.2 and
458 3.7 Å (Fig. 12; Table 5). The Mn1 shell has been observed previously in δ -MnO₂ and manganite
459 (γ -MnOOH), and was interpreted as an edge-sharing (ES) complex (Matocha et al., 2001; Morin
460 et al., 2001). In ferrihydrite, in which the ES complex also occurs, the Pb-Fe interaction is about
461 0.1 Å larger (i.e., 3.3 Å) than the Pb-Mn interaction in δ -MnO₂, a value that matches the
462 difference in effective ionic radii between Mn(IV) and Fe(III) (0.53 vs 0.64 Å). Since δ -MnO₂
463 has a layered structure and its crystallites have a small lateral extension (i.e., low crystallinity),
464 the ES complex is located probably at layer edges and is presumably tridentate (Fig. 14). The
465 Mn2 shell has been reported previously in well-crystallized birnessite and attributed to a
466 tridentate corner-sharing complex (TCS) in the interlayer (Manceau et al., 1999; 2002a; Morin et
467 al., 1999; Matocha et al., 2001). This structural interpretation was confirmed subsequently by
468 electron and X-ray diffraction (Drits et al., 2002; Lanson et al., 2002a). At this interlayer position,
469 the Pb atoms are bonded to three O atoms from a vacant octahedral site of the Mn oxide layer,
470 thus helping to balance the charge deficiency of the layer created by Mn(IV) vacancy sites (Fig.
471 14).

472 Consideration of a Mn3 shell at 4.09 Å in PbBi31 better replicated the data than the single
473 Mn2 shell model, in particular in the $9 < k < 11 \text{ \AA}^{-1}$ interval (Fig. 12k, Table 5). This second shell
474 was not resolved in our previous study (Manceau et al., 2002a) because the EXAFS data were
475 limited to $k < 10 \text{ \AA}^{-1}$. The magnitude of the distance separation between the Mn2 and Mn3 shells
476 ($4.09 - 3.70 = 0.39 \text{ \AA}$) is similar to that in quenselite ($3.96 - [(3.57 + 3.43)/2] = 0.46 \text{ \AA}$;
477 PbMnO₂OH) (Rouse, 1971) and, by analogy with the structure of this mineral, the six nearest
478 Pb-Mn distances from the TCS complex likely are unequal. The incoherency of the Pb-Mn
479 distances in Pb-sorbed birnessite explains the apparent loss of coordination since an effective
480 number of $N = 1.0 + 0.8 = 1.8$ Mn atoms are detected instead of a crystallographic number of CN
481 = 6 (Fig. 11).

482 Another distinction among the reference spectra is a 0.04 Å reduction of the average Pb-O
483 distance in PbBi31 and PbdBi197 relative to PbdBi2, PbdBi44, and PbdBi35 (Table 5). Since the
484 first group of samples has a higher ES/TCS ratio, the ES complex presumably has a longer
485 average Pb-O distance than the TCS complex. This increase in distance can be explained by the
486 higher electrostatic repulsion between Pb(II) and Mn(IV) at the edge-sharing site (shorter Pb-Mn
487 distance) than at the corner-sharing site (longer Pb-Mn distance). This effect was detected
488 because the proportion of TCS complex is low at low surface coverage.

489 Finally, the proportion of ES and TCS complexes in AD14 was estimated from the effective
490 number of Pb-Mn1 and Pb-Mn2 pairs ($N = 0.2$ and 0.6 , respectively; Table 5) and the
491 crystallographic number of nearest Mn neighbors at site TCS ($CN = 6$) and ES ($CN = 2$) (Fig. 14).
492 According to this calculation, Pb is evenly distributed over the two sites.

493

494

4. DISCUSSION

495

4.1. Ce anomaly

497

498 Cerium L_{III}-edge XANES data showed that Ce is exclusively tetravalent in all samples,
499 regardless of genetic origin. In general, Ce oxidation is considered to be responsible for the
500 positive Ce anomaly in REE patterns of ferromanganese oxides (e.g., Takahashi et al., 2000).

501 The rationale is that Ce(IV) is taken up preferentially over Ce(III) by solid phases in contact with
502 seawater because Ce(IV) is much less soluble than Ce(III). This explanation does not seem to be
503 valid for diagenetic and hydrothermal ferromanganese oxides because they have a negative, or at
504 best moderately positive, Ce anomaly when the data are normalized to PAAS (shale), as is often
505 observed (Fig. 2a). Figure 2b shows that this discrepancy disappears when the REE
506 concentrations in the solid phase are normalized to their abundances in deep seawater (Piepgras

507 and Jacobsen, 1992). In doing this, the Ce anomalies are all positive, which agrees with the
508 dominance of Ce(IV) in all samples (Fig. 2b). The reason is that REE in deep seawater, where
509 hydrogenetic nodules occur, are more strongly depleted in Ce than the more reducing interstitial
510 and hydrothermal waters, where the two other types of ferromanganese oxides occur. Also, Ce
511 normalization by PAAS is unsuitable because Ce is not removed by the same geochemical
512 processes in shales and marine nodules.

513 If we assume that Ce(III) in ferromanganese oxides is in equilibrium with Ce(III) in water,
514 and that Ce(III) is the only soluble species, then the normalized abundance of Ce(III) in the solid
515 phase, denoted Ce^* , can be obtained from the interpolation of the normalized abundances for La
516 and Pr: $(Ce^*)_{SW} = (La^{1/2}Pr^{1/2})_{SW}$, where SW stands for normalization by REE abundances in
517 seawater. The $(Ce^*/Ce_{total})_{SW}$ ratio calculated for FG352 is 15 %, and could be detected by
518 XANES spectroscopy. This ratio is a maximum value among the samples examined, because this
519 sample has the lowest Ce anomaly in the dataset (Fig. 2b). The $CeCl_3 : Ce(SO_4)_2$ spectrum in
520 Figure 5 shows that 10 % of Ce(III) in a mixed-valence sample manifests itself in the appearance
521 of a shoulder at 5724 eV. None of the sample spectra have such a shoulder including FG352.
522 Also, the maximum of the 1st derivative of this composite spectrum is at 5724.4 eV, while this
523 maximum is between 5726 and 5727 eV in the sample spectra and Ce(IV) references. This
524 analysis confirms the lack of detectable Ce(III) in ferromanganese oxides, even in a sample
525 having a weak Ce anomaly. Therefore, Ce(III) is completely oxidized to Ce(IV) in
526 ferromanganese oxides, and the magnitude of the positive Ce anomaly is not related to a
527 variation of redox conditions, but probably to kinetic factors, as discussed below.

528

529 **4.2. Ce and Co incorporation in ferromanganese oxides**

530

531 Homogeneous precipitation and formation of Ce oxide in marine sediments have been
532 proposed for Ce(IV) removal from seawater (e.g., De Carlo and McMurtry, 1992; Ohta et al.,

1999; Haley et al., 2004). This mechanism can be dismissed because none of the XANES spectra of the samples resemble those of CeO_2 and Ce(OH)_4 . Therefore, oxidative sorption of dissolved Ce(III) likely is the main pathway of Ce incorporation in ferromanganese oxides. Since Ce(IV) is sparingly soluble (De Baar et al., 1988; Byrne, 2002), the sorbate remains at the surface of the Fe-Mn oxide after oxidation took place, leading progressively to Ce enrichment. Based on the low amount of Ce in seawater and the nanometer size of the ferrihydrite and manganese particles (Villalobos et al., 2006), saturation of reactive surface sites by Ce(IV) is unlikely to occur. Also, the exposed surface is progressively buried during the growth of the ferromanganese oxide. This process controls the Ce enrichment, and prevents poisoning of the surface, as observed in the laboratory at high sorbate - metal sorbent ratio (Manceau et al., 1997). Therefore, Ce enrichment must be controlled by the growth rate of the ferromanganese oxide, as suggested for Co (Halbach et al., 1983; Mannheim and Lane-Bostwick, 1988; Takematsu et al., 1989). Consistent with this interpretation, the growth rate of ferromanganese oxides increases in the order hydrogenetic < diagenetic < hydrothermal oxides (Dymond et al., 1984), while the degree of Ce anomaly (and REE content) decreases in the reverse order. The fact that the Fe/Mn ratio varies with the Ce anomaly does not mean that Ce is associated with the Fe oxide component.

This geochemical interpretation of the Ce partitioning at the Mn oxide - water interface can be extended to cobalt, since this element is divalent in seawater (Byrne, 2002), oxidized to Co(III) by Mn oxides (Murray and Dillard, 1979), sparingly soluble in its oxidized form, systematically present as Co(III) in the three genetic-type oxides, and less abundant in fast growing ferromanganese oxides (Halbach et al., 1983; Mannheim and Lane-Bostwick, 1988). Co(III) is substituted isomorphically for Mn in the manganese layer (Manceau et al., 1987, 1997), and the steric match between Co(III) (0.54 Å) and Mn(IV) (0.53 Å) is believed to be responsible for the selective enrichment of cobalt in manganese oxides (Burns, 1976). The nature of the Ce incorporation site in phylломanganates is unknown. With a size of 0.80 Å in octahedral coordination, Ce(IV) is too big to occupy Mn layer site, but may reside in the interlayer on top of

559 vacant Mn layers sites commonly observed in metal-containing birnessite (Drits et al., 2002;
560 Lanson et al., 2002a; Manceau et al., 2002a).

561

562 **4.3. Pb surface complexation on ferrihydrite**

563

564 EXAFS results show that Pb forms the same type of surface complex on marine ferrihydrite
565 as in the laboratory. Pb sorption on synthetic ferrihydrite at pH 6.5 was modeled by Manceau et al.
566 (1992b) by two nearest oxygen subshells at 2.22 and 2.42 Å, and two next-nearest iron subshells
567 of 0.3 Fe at 3.29 Å and 0.4 Fe at 3.45 Å. The two Pb-O (2.38 and 2.65 Å) and Pb-Fe (3.32 and
568 3.50 Å) distances reported here are similar to those inferred in our past spectroscopic study. The
569 new values are more accurate because the Pb-EXAFS spectrum from the previous study had a
570 lower signal-to-noise ratio and k range. The Pb-O distances are similar to those in β -PbO (2.21
571 and 2.49 Å; Leciejewicz, 1961) and, by analogy with the coordination of Pb(II) in this compound,
572 lead atoms are assumed to be at the apex of a distorted pyramid. The Pb-Fe distances are
573 interpreted by the formation of an ES surface complex, and their bimodal distribution as the
574 consequence of the split of the Pb-O distances in the first shell. Similar geometry was reported
575 for lead sorption on goethite and hematite (Bargar et al., 1997b, 1998). The formation of an ES
576 complex on synthetic ferrihydrite was confirmed by Scheinost et al. (2001), who reported an Fe
577 coordination about Pb of one at a distance of 3.32 Å at pH 5.0. In this last study, the local
578 structure of Pb was invariant with the reaction time (up to 2 months), ferrihydrite morphology
579 (with and without freeze-drying), metal competition (Cu^{2+}), and fulvic acid concentration.
580 Similarly, Trivedi et al. (2003) reported an average Pb-Fe distance of 3.34 Å on ferrihydrite at pH
581 5.5 and 6.5. While the resolution in interatomic distance was lower in the studies of Scheinost et
582 al. (2001) and Trivedi et al. (2003), all of the above results collectively support the formation of
583 edge-sharing lead complex on ferrihydrite, regardless of its origin and formation conditions. In
584 particular, there is no spectroscopic evidence for the existence of Pb-Cl pairs in natural samples

585 and, hence, for the formation of a Pb-Cl-Fe ternary surface complex, despite the high activity of
586 chlorine (0.54 M) in seawater. This finding was predicted from laboratory studies (Balistrieri and
587 Murray, 1982; Bargar et al., 1998).

588

589 **4.4. Pb surface complexation on phylломanganate**

590

591 Two short distance Pb-Mn pairs were identified, one at 3.2 Å and another at 3.7 Å,
592 corresponding to ES and TCS complexes, respectively. The ES complex occurs at layer edges
593 (Morin et al., 2001) and the TCS complex in the interlayer (Manceau et al., 1999, 2002; Morin et
594 al., 1999; Matocha et al., 2001). The detection of the ES complex at low Pb loading in δ -MnO₂
595 indicates that it has a high affinity for the phylломanganate surface. This complex likely occurs
596 in PbBi31, but its fractional amount relative to the TCS complex is negligible because PbBi31
597 contains 15 times more Pb than PbdBi2, and its particles have a larger lateral size (i.e., better
598 crystallinity). Their lateral dimension, as estimated by X-ray diffraction from the size of coherent
599 scattering domains (CSD), is ~ 200 Å (Lanson et al., 2002a) compared to 60 Å for δ -MnO₂
600 (Villalobos et al., 2003), consistent with Brunauer-Emmett-Teller (BET) measurements, showing
601 that the well-crystallized birnessite particles have an external (N₂) specific surface area of 27
602 m²/g (Manceau and Charlet, 1992) vs. 120-150 m²/g for δ -MnO₂ (Villalobos et al., 2003).

603 The higher affinity of lead for lateral sites cannot be explained by a higher number of
604 Pb-O-Mn bonds at these sites since in the proposed structural model (Fig. 14) lead is coordinated
605 to three surface oxygens on both interlayer and external sites (i.e., formation of a tridentate
606 complex on both sites). The reason may be electrostatic in nature. Because the three oxygens
607 from a vacant octahedral site are doubly coordinated to layer Mn, the total charge deficit at a
608 TCS site is $3x[(-2) + 2x(4^+/6)] = -2$ v.u. Thus, sorption of two protons or one Pb²⁺ at a TCS site
609 compensates the charge deficit on either side of a Mn(IV) vacancy (Silvester et al., 1997). In
610 contrast, the ES site has two oxygens singly coordinated to bulk Mn atoms and one doubly

611 coordinated (Fig. 14). The total charge at an ES site is $2x[(-2) + (4^+/6)] + [(-2) + 2x(4^+/6)] = -3.3$
 612 v.u. Its charge compensation requires the sorption of one Pb^{2+} and one or two protons. Then, the
 613 high reactivity of lateral sites towards metal sorption can be viewed as the consequence of the
 614 lamellar structure of δ - MnO_2 and the nanometer size of the particles (high external to internal
 615 surface ratio). One may argue that basal sites should be preferred over lateral sites since
 616 conjoined edges have significantly more Pb^{2+} - Mn^{4+} repulsion (shorter Pb-Mn distance) than TCS
 617 sites. However, lateral sites have less steric restriction than basal sites because two of the three
 618 surface oxygens are singly coordinated in the first case, whilst they are all doubly coordinated in
 619 the second.

620

621 **4.5. Evaluation of the formation of DCS complexes at layer edges**

622

623 The progressive reduction in amplitude of the TCS Pb-Mn peak ($d(Pb-Mn_2) = 3.7 \text{ \AA}$) with
 624 decreasing Pb/Mn ratio (Fig. 13b) is interpreted as the preponderance of a high surface-affinity
 625 ES complex ($d(Pb-Mn_1) = 3.2 \text{ \AA}$) at low surface coverage. This evolution also has been
 626 interpreted by the existence of a double-corner sharing (DCS) complex on layer edges with a
 627 Pb-Mn distance of 3.50 - 3.55 \AA (Villalobos et al., 2005). In this alternative model, the TCS and
 628 DCS sites were supposed to be occupied concurrently and independently of the Pb/Mn ratio,
 629 meaning that Pb had the same affinity for external (DCS) and internal (TCS) sites. As explained
 630 below, this structural interpretation is problematic.

631 In the DCS+TCS model of Villalobos et al. (2005), the data were fit with the following
 632 assumptions. First, Pb forms a DCS complex ($CN = 2$) at layer edges and a TCS complex ($CN =$
 633 6) in interlayers. This predetermined structural model was used in the spectral simulations to
 634 constrain the EXAFS numbers (N) of Mn neighbors at each site to the Pb occupancy (f_{ext} and f_{int} ,
 635 with $f_{ext} + f_{int} = 1$), such that $N(DCS) = 2 \times f_{ext}$ and $N(TCS) = 6 \times f_{int}$. For example, if Pb was
 636 evenly distributed among the two sorption sites, then $N(DCS) = 2 \times 0.5 = 1.0$, and $N(TCS) = 6 \times$

637 0.5 = 3. Second, the structural disorder is anharmonic in the O shell ($N(\text{EXAFS}) < CN$) and
 638 harmonic in the Mn shells ($N(\text{EXAFS}) = CN$). This assumption is incorrect for the immense
 639 majority of Pb compounds, including sorption complexes (Manceau et al., 1996; Bargar et al.,
 640 1997a). In practice, this model reproduced the data fairly well (Fig. 12j), but with generally
 641 meaningless values (e.g., $\sigma = 0.16 \text{ \AA}$) for the Debye-Waller parameter (the harmonic model
 642 becomes questionable when σ is higher than $\sim 0.10 \text{ \AA}$; Teo, 1986; Crozier, 1997). With one
 643 exception this disorder parameter was arbitrarily fixed to a lower value for the more distant TCS
 644 shell than for the DCS shell, as if the structural disorder in solid matter could decrease with radial
 645 distance. Still another problem with the DCS+TCS model is the unrealistically large interval of
 646 variation of the energy threshold parameter ($-21 \leq \Delta E_0 \leq -13 \text{ eV}$). In a binary system, this
 647 parameter should be constant, both for physical reasons and to decrease the degree of freedom
 648 (Schlegel et al., 2001), otherwise non-linear least-squares fits converge to local minima and,
 649 hence, to erroneous structural solution.

650 Consequently, the physical and mathematical problems with the DCS+TCS model are
 651 believed to be the reasons for the misidentification of the ES complex at 3.2 \AA as a DCS complex
 652 at $3.50\text{-}3.55 \text{ \AA}$. To test this hypothesis, the PbBi31 spectrum was fit successively with the TCS
 653 (Fig. 12i) and the DCS+TCS (Fig. 12j) models. This sample contains major TCS and minor ES
 654 complexes because it has 15 times more Pb than PbdBi2, and its particles have a large lateral
 655 dimension. The TCS model ($R = 3.72 \text{ \AA}$, $N = 1.3$, $\sigma^2 = 0.008 \text{ \AA}^2$) and the DCS + TCS model ($R =$
 656 3.46 \AA , $N = 1.0$, $\sigma^2 = 0.014 \text{ \AA}^2 + R = 3.70 \text{ \AA}$, $N = 3.0$, $\sigma^2 = 0.014 \text{ \AA}^2$) equally reproduced the data
 657 ($Rp = 24$, Table 5), and accounted for the major spectral features. This apparently anomalous
 658 result has a simple explanation.

659 Consider an EXAFS signal consisting of waves from two shells as in the DCS+TCS model,
 660 with the shells differing only in distance and coordination number. A simplified representation of
 661 this signal is given by

$$662 \quad \chi = A(k) \exp(2ikR + \delta(k))(1 + a \exp(2ik\Delta r))$$

663 where A and δ are the usual single-scattering EXAFS terms, a is the ratio of amplitudes of the
 664 two shells, R the distance for the stronger shell (TCS), and Δr the distance difference. In our case,
 665 $a = 1/3$ since $f_{\text{ext}} = f_{\text{int}}$, $R = 3.70 \text{ \AA}$, and $\Delta r = -0.24 \text{ \AA}$. For these values, the phase difference $2k\Delta r$
 666 is π at $k = 6.5 \text{ \AA}^{-1}$ and, the two waves interfere destructively over most of the data range (Fig. 15).
 667 This makes the coordination number appear small, and the FT peak low in amplitude. However, it
 668 is not obvious that the sum of the two waves really looks like a single wave. We can show that it
 669 does by considering the phase difference between the combined signal (DCS + TCS model) and
 670 that from a single wave (TCS model) with distance R :

$$671 \quad \Delta\phi = \arg(1 + a \exp(2ik\Delta r))$$

672 If we draw an Argand diagram (phasor plot), we see that as a function of k , this phase difference
 673 oscillates between limits of $\pm \sin^{-1} a$, which is about 19° (0.34 rad) here. The extrema occur
 674 when $2k\Delta r = \pi \pm (\pi/2 - \sin^{-1} a)$. In our case, $\Delta R = 0.24 \text{ \AA}$, so these points occur at $k = 4$ and 9.1
 675 \AA^{-1} , approximately bracketing the range where the signal is largest. Thus, within that range, there
 676 is an approximately linear phase difference between the DCS + TCS and TCS-only signals,
 677 which can be compensated for in the data fitting by adjusting the assumed distance (i.e., 3.70 vs.
 678 3.72 \AA) and energy origin (i.e., $\Delta E_0 = -7$ vs -5 eV, Table 5). The above argument even accounts
 679 for the distance in the TCS model fit (3.72 \AA) being greater than the greater of the two distances
 680 in the DCS + TCS model (3.70 \AA). The phase difference $\Delta\phi$ is negative for $k < \pi/(2\Delta R)$, zero at k
 681 $= \pi/(2\Delta R)$, where the shells are exactly out of phase, and positive for $k > \pi/(2\Delta R)$, which is the
 682 effect provided by a distance increase over R , plus a small adjustment of the energy origin ΔE_0 .
 683 Similarly, the amplitude can be shown to be approximately (within the goodness of the fit to
 684 TCS-only) described by a change of mean-square relative deviation (i.e., σ value). We see that
 685 unless the data are taken over a large k -range and fit to very good models, it can be impossible to
 686 tell the difference between a single shell (TCS model) and a pair of shells (DCS + TCS model) of
 687 different coordination numbers and distances. Here, the correct model (ES + TCS) was

688 determined by varying experimentally the Pb/Mn ratio over two orders of magnitude (0.002
689 $< \text{Pb/Mn} < 0.197$ in the $\delta\text{-MnO}_2$ series) compared to a factor of 5 ($0.035 \leq \text{Pb/Mn} \leq 0.174$) in
690 Villalobos et al. (2005), and by constraining the variation range of the fit parameters to physically
691 meaningful values.

692

693 **4.6. Pb partitioning among Mn and Fe oxide**

694

695 With a Mn/Fe weight ratio of 1.04 (Table 2) and a Mn-bound to Fe-bound lead ratio of
696 approximately 1, lead is unfractionated between the two oxides in D21-m3. In contrast, it is
697 moderately partitioned in the Mn oxide in D1-X1 (Mn/Fe = 0.3; Mn-bound/Fe-bound ≈ 1), and
698 strongly partitioned in AD14 (Mn/Fe = 1.1; Mn-bound/Fe-bound > 9). The sorption of Pb on
699 both Fe and Mn oxide in D21-m3 and D1-X1 can be explained by the fact that conjoined edge
700 sites also exist at chain terminations in ferrihydrite (Drits et al., 1993) which also have a high
701 affinity for cations (Spadini et al., 1994). Therefore, tridentate sites at chain terminations in Fe
702 oxide and at layer edges in Mn oxide may sorb lead equally in marine ferromanganese oxides.
703 The similarity of the O-O conjoined edge distances for FeO_6 octahedra (2.59 Å; Szytula et al.,
704 1968) and MnO_6 octahedra (2.62 Å; Lanson et al., 2002b) also explains the ability of the two
705 oxides to complex Pb(II) adions in tridentate edge-sharing geometries. Fe oxides may also bind
706 metal adions in bidentate edge-sharing geometries (i.e., sharing of only one edge with a single
707 octahedron), but apparently the energy stabilization gained from forming multiple edge bonds to
708 the Fe oxide surface is higher (Spadini et al., 2003). In summary, from a structural standpoint,
709 lead may sorb on either oxide, and its strong partitioning in AD14 does not have a simple
710 structural explanation.

711 It has been suggested that lead is associated with the Fe oxide component in marine
712 ferromanganese oxides because Pb is speciated as neutral or negatively charged moieties, such as

713 $\text{Pb}(\text{CO}_3)_n^{(2-2n)-}$ ($n>1$), and because Fe oxides have a net positive charge and Mn oxides a net
714 negative charge at circumneutral pH (Stumm, 1993; Koschinsky and Halbach, 1995; Langmuir,
715 1997; Koschinsky and Hein, 2003). This electrostatic explanation to geochemical partitioning on
716 Fe oxide is satisfying for anionic species, such as AsO_3^{3-} and AsO_4^{3-} (e.g., Smedley and
717 Kinniburgh, 2002; Koschinsky and Hein, 2003), but not for Pb because cationic moieties (Pb^{2+} ,
718 PbCl^+ , and PbOH^+) co-exist with neutral and negative species in seawater according to chemical
719 equilibrium calculations. Three explanations can be proposed for Pb sorption on Fe and Mn
720 oxides in seawater. First, cationic lead species preferentially sorb on Mn oxide and anionic lead
721 species on Fe oxide. Second, sorption of cationic Pb species on Mn oxide shifts chemical
722 equilibrium in direction of the dissociation of anionic Pb complexes, thus leading to Pb
723 enrichment on Mn oxide. Third, the chemical (i.e., binding) component of the free energy for
724 tridentate Pb(II) sorption to octahedral edges on both oxides is much larger than the electrostatic
725 component. In this case a charged adion is sorbed specifically regardless of the sign of the surface
726 charge (Anderson and Rubin, 1981). Since Pb can be taken up by Mn and Fe oxides in the marine
727 environment, the Pb – Fe/Mn correlation in Fig. 1b does not mean that Pb is chemically bound to
728 the Fe oxide component, but that its enrichment depends on the growth rate of the
729 ferromanganese oxide, as for Ce and Co.

730 Independent of the geochemical partitioning of Pb between Mn and Fe oxide, both oxides
731 have strong binding sites that must be able to retain Pb over long periods of time because
732 ferromanganese deposits have a slow growth rate (mm/Myr) (e.g., Halbach et al., 1983; Halbach
733 et al., 1988; Takematsu, 1998). Knowing the molecular mechanism of Pb sequestration in these
734 deposits is essential to understand its marine geochemistry, and in particular its enrichment by up
735 to a factor of 200 relative to its crustal abundance (8.0 mg/kg; Faure, 1998) and 7×10^8 relative
736 to seawater concentration (1.3×10^{-11} M; Schaule and Patterson, 1981). This knowledge is also
737 important for environmental contamination issues because ferrihydrite and vernadite (the generic
738 term for natural turbostratic phyllosulfate; Manceau et al., 2006) are ubiquitous in soils and

739 continental sediments (Chukhrov and Gorshkov, 1981; Dixon and Skinner, 1992; Davison, 1993;
740 Manceau et al., 2003, 2005; Vodyanitskii and Sivtsov, 2004; Hochella et al., 2005a), and because
741 the lead-ferrihydrite / lead-vernadite co-association (D21-m3, D1-XA) and the lead-vernadite
742 partitioning (AD14) described here are common (Mckenzie, 1989; Hudson-Edwards, 2000;
743 Latrille et al., 2001; Liu et al., 2002; Cornu et al., 2005; Hochella et al., 2005b). Therefore, this
744 work provides context for further studies on the sequestration mechanism of Pb at Earth's
745 surface.

746

747 **4.7. Redox reactions of Ce, Co, and Pb sorbed on ferromanganese oxides**

748

749 Although Co and Ce have similar geochemical behavior in the marine environment (Addy,
750 1979; Ohta et al., 1999), some differences exist that are related to their redox properties. Ce and
751 Co are both readily oxidized by manganates, but while Ce may be oxidized also by Fe
752 oxyhydroxides (e.g., Bau, 1999; Kawabe et al., 1999), Co is not (e.g., Coughlin and Stone, 1995;
753 Angove et al., 1999; Jeon et al., 2003; Pozas et al., 2004). The redox potential of the
754 Ce(III)/CeO₂ couple in seawater is about $E_h = 178\text{-}237$ mV ($p\varepsilon = 3\text{-}4$; De Baar et al., 1988). The
755 redox potential of the Co²⁺/CoOOH couple at pH 8, $\text{Co}^{2+}_{(\text{aq})} = 2.0 \times 10^{-11}$ M (the dissolved Co
756 concentration in seawater; Martin et al., 1989), and $E^0 = 1.48$ V (Moffett and Ho, 1996), is 689
757 mV. Thus, Ce(III) is easily oxidized in seawater, even by dissolved oxygen (De Baar et al., 1988),
758 whereas Co(II) is only oxidized by MnO₂ (Murray and Dillard, 1979; Manceau et al., 1997).

759 Thermodynamic considerations also help understand the lack of oxidation of Pb(II) to
760 Pb(IV) in marine ferromanganese oxides. The potential of the Pb²⁺/PbO₂ couple is 837 mV,
761 based on Brookins' data (1988) and a Pb_(aq) concentration in seawater of 1.3×10^{-11} M (Schaulé
762 and Patterson, 1981). This value is greater than the potential of H₂O/O₂ at P_{O₂} = 1 atm and pH 8
763 (756 mV), meaning that Pb(II) cannot be oxidized to Pb(IV) in homogeneous condition within

764 the stability field of water. Catalytic Pb(II) oxidation at the phyllosulfate surface could occur
765 (Murray and Dillard, 1979), but XANES and EXAFS spectroscopic data show that it does not
766 (Matocha et al., 2001; Manceau et al., 2002a; Takahashi et al., 2002b; Villalobos et al., 2005).
767 According to thermodynamic calculations, Pb(II) oxidation could be mediated by hausmannite
768 (Mn_3O_4 ; Hem, 1978), but this mixed-valence Mn oxide with a spinel structure has never been
769 identified in marine ferromanganese oxides.

770 Thus, it can be argued that the partitioning of the three redox-sensitive trace metals depends
771 on their redox potential. Since Co(II) is oxidized exclusively by Mn(III) and Mn(IV), and is
772 present as Co(III) in marine ferromanganese oxides, then this element can be anticipated to be
773 strictly associated with Mn oxides, as is shown by ample experimental evidence. Ce, which is
774 immobilized also in its oxidized form, probably is associated predominantly with Mn oxides
775 because Mn(IV) is a strong oxidant at pH 8.3. However, Ce(IV) - Fe oxide associations may also
776 occur, as Ce(III) can be oxidized by oxygen and freshly precipitated Fe oxides (Bau, 1999). This
777 association is not widespread because it is inhibited kinetically by the slow rate of Ce(III) to
778 Ce(IV) oxidation by O_2 and Fe(III). Of the three trace metals studied here, Pb probably has the
779 lowest affinity for Mn oxides, since it is always divalent. This hypothesis is supported by EXAFS
780 data, which show that Pb is associated partly with Fe in two of the three samples examined, and
781 re-adsorbed on the Fe component when the Mn component is dissolved. The lesser affinity of Ce
782 and Pb for the Mn oxide component compared to Co likely accounts for the weak Ce - Mn/Fe and
783 Pb - Mn/Fe correlations measured by EPMA (Fig. 4). Consistent with our hypothesis, the
784 correlation between Co and Mn/Fe is strong.

785
786 *Acknowledgment* - We thank Dr. T. Kuhn for providing GTV samples and for his comments
787 on an earlier version of the manuscript. The following colleagues are also thanked for their
788 advice and technical assistance in the laboratory and at synchrotron facilities: S. Fakra, M.
789 Fukukawa, J.L. Hazemann, H. Ishisako, N. Kishikawa M. Murakami, M. Nomura, O. Proux, N.

790 Sakakibara, Y. Shibata, Y. Shimamoto, and T. Uruga. The final version of the manuscript
791 benefited from the careful reviews by three anonymous referees. We thank the Geological Survey
792 of Japan (GSJ), the US Geological Survey (USGS), and the Metal Mining Agency of Japan for
793 providing samples. This research was supported by a grant-in-aid for scientific research from the
794 Ministry of Education, Science, Sports, and Culture of Japan. This work has been performed with
795 the approval of KEK (Proposal No. 2000G267), JASRI (Proposal No. 2000B0276), and the
796 French-CRG program of the CNRS at ESRF. The ALS is supported by the Director, Office of
797 Energy Research, Office of Basic Energy Sciences, Materials Sciences Division of the U.S.
798 Department of Energy, under Contract No. DE-AC02-05CH11231.

REFERENCES

- 799
- 800
- 801 Addy, S.K., 1979. Rare earth element patterns in manganese nodules and micronodules from
802 northwest Atlantic. *Geochim. Cosmochim. Acta* **43**, 1105-1115.
- 803 Akagi, T., Masuda, A., 1998. A simple thermodynamic interpretation of Ce anomaly. *Geochem. J.*
804 **32**, 301-314.
- 805 Ambe, S., Chen, S.Y., Ohkubo, Y., Kobayashi, Y., Maeda, H., Iwamoto, M., Yanokura, M.,
806 Takematsu, N., Ambe, F., 1995. "Multitracer" a new tracer technique - its principle, features,
807 and application. *J. Radioanal. Nucl. Chem.* **195**, 297-303.
- 808 Anderson, M.A., Rubin, A.J., 1981. Adsorption of inorganics at solid-liquid interfaces. Ann Arbor
809 Science Publishers, Inc.
- 810 Angove, M.J., Wells, J.D., Johnson, B.B., 1999. The influence of temperature on the adsorption
811 of cadmium(II) and cobalt(II) on goethite. *J. Colloid Interface Sci.* **211**, 281-290.
- 812 Ankudinov, A.L. Rehr, J.J., 1997. Relativistic spin-dependent X-ray absorption theory, *Phys. Rev.*
813 *B* **56**, 1712-1715.
- 814 Aplin, A.C., Cronan, D.S., 1985a. Ferromanganese oxide deposits from the Central Pacific
815 Ocean. I. Encrustations from the Line Islands Archipelago. *Geochim. Cosmochim. Acta* **49**,
816 427-436.
- 817 Aplin, A.C., Cronan, D.S., 1985b. Ferromanganese oxide deposits from the Central Pacific
818 Ocean. II. Nodules and associated sediments. *Geochim. Cosmochim. Acta* **49**, 437-451.
- 819 Balistrieri, L.S., Murray, J.W., 1982. The adsorption of copper, lead, zinc, and cadmium on
820 goethite from major ion seawater. *Geochim. Cosmochim. Acta* **46**, 1253-1265.
- 821 Bargar, J.R., Brown, G.E. Jr., Parks, G.A., 1997a. Surface complexation of Pb(II) at oxide-water
822 interfaces: I. XAFS and bond-valence determination of mononuclear and polynuclear Pb(II)
823 sorption products on aluminum oxides. *Geochim Cosmochim Acta* **61**, 2617-2637.

- 824 Bargar, J.R., Brown, G.E. Jr., Parks, G.A., 1997b. Surface complexation of Pb(II) at oxide-water
825 interfaces: II. XAFS and bond-valence determination of mononuclear and polynuclear Pb(II)
826 sorption products on iron oxides. *Geochim Cosmochim Acta* **61**, 2639-2652.
- 827 Bargar, J.R., Brown, G.E. Jr., Parks, G.A., 1998. Surface complexation of Pb(II) at oxide-water
828 interfaces: III. XAFS determination of Pb(II) and Pb(II)-chloro adsorption complexes on
829 goethite and alumina. *Geochim. Cosmochim. Acta*, **62**, 193-207.
- 830 Bau, M., 1999. Scavenging of dissolved yttrium and rare earths by precipitating iron
831 oxyhydroxide: Experimental evidence for Ce oxidation, Y-Ho fractionation, and lanthanide
832 tetrad effect. *Geochim. Cosmochim. Acta*, **63**, 67-77.
- 833 Betekhtin A. G. (1940) South Urals manganese deposits as a raw material base for the
834 Magnitogorsk metallurgic plant. *Trudi Inst. Geol. Sci. Acad. Sci. USSR, Ore deposit Ser.*
835 N° 4.
- 836 Bianconi, A., 1988. XANES spectroscopy. In: Koningsberger, D.C., Prins, R (Eds), *X-ray*
837 *Absorption. Principles, Applications, Techniques of EXAFS, SEXAFS and XANES*. John Wiley,
838 New York, p 573-662.
- 839 Brookins, D.G., 1988. *Eh-pH Diagrams for Geochemistry*. Springer-Verlag, Berlin.
- 840 Burns, R.G., 1976. The uptake of cobalt into ferromanganese nodules, soils, and synthetic
841 manganese(IV) oxides. *Geochim. Cosmochim. Acta* **40**, 95-102.
- 842 Byrne, R.H., 2002. Inorganic speciation of dissolved elements in seawater: the influence of pH
843 on concentration ratios. *Geochem. Trans.* **3**, 11-16.
- 844 Calvert, S.E. Piper, D.Z., 1984. Geochemistry of ferromanganese nodules from DOMES Site A,
845 Northern Equatorial Pacific: Multiple diagenetic metal sources in the deep sea. *Geochim.*
846 *Cosmochim. Acta* **48**, 1913-1928.
- 847 Choi, Y.G., Kim, K.H., Chernov, V.A., Heo, J., 1999. Pb L_{III}-edge EXAFS and XANES analyses
848 on the structural environment of lead in PbO-Ga₂O₃ glasses. *J. Non-Cryst. Solids* **246**,
849 128-135.

- 850 Chukhrov, F.V., Gorshkov, A.I., 1981. Iron and manganese oxide minerals in soils. *Trans. of*
851 *Royal Soc., Edinburg*, **72**, 195-200.
- 852 Cornu, S., Deschatrettes, W., Salvador-Blanes, S., Clozel, B., Hardy, M., Branchut, S., Le
853 Forestier, L., 2005. Trace element accumulation in Mn-Fe-oxide nodules of a planosolic
854 horizon. *Geoderma* **125**, 11-24.
- 855 Coughlin, B.R. Stone A.T., 1995. Nonreversible adsorption of divalent metal ions (Mn^{II} , Co^{II} , Ni^{II} ,
856 Cd^{II} , and Pb^{II}) onto goethite: Effects of acidification, Fe^{II} addition, and picolinic acid addition.
857 *Environ. Sci. Technol.* **29**, 2445-2455.
- 858 Crozier, E.D., 1997. A review of the current status of XAFS spectroscopy. *Nucl Instrum Meth*
859 *Phys Res* **B133**, 134-144.
- 860 Davison, W., 1993. Iron and manganese in lakes. *Earth Sci. Reviews* **34**, 119-163.
- 861 De Baar, H.J.W, German, R.C., Elderfield, H., Van Gaans, P., 1988. Rare earth elements
862 distributions in anoxic waters of the Cariaco Trench. *Geochim. Cosmochim. Acta* **52**,
863 1203-1219.
- 864 De Carlo, E.H., McMurtry, G.M., 1992. Rare-earth element geochemistry of ferromanganese
865 crusts from the Hawaiian Archipelago, Central Pacific. *Chem. Geol.* **95**, 235-250.
- 866 Dillard, J.G., Koppelman, M.H., Crowther, D.L., Schenk, C.V., Murray, J.W., Balistrieri, L., 1981.
867 X-ray photoelectron spectroscopic (XPS) studies on the chemical nature of metal ions
868 adsorbed on clays and minerals. In: Tewari, P.H. (Ed.), *Adsorption From Aqueous*
869 *Solutions*, Plenum Press, New York, pp. 227-240.
- 870 Dillard, J.G., Crowther, D.L., Murray, J.W., 1982. The oxidation states of cobalt and selected
871 metals in the Pacific ferromanganese nodules. *Geochim. Cosmochim. Acta* **46**, 755-759.
- 872 Dixon, J.B., Skinner, H.C.W., 1992. Manganese minerals in surface environments. In: Skinner,
873 H.C.W., Fitzpatrick, R.W. (Eds), *Biomineralization processes of iron and manganese. Modern*
874 *and ancient environments*. CATENA Verlag. pp. 31-50.
- 875 Drits, V.A., Sakharov, B.A., Salyn, A.L., Manceau, A., 1993. Structural model for ferrihydrite.

- 876 *Clay Mineral.* **28**, 185-208.
- 877 Drits, V.A., Lanson, B., Bougerol-Chaillout, C., Gorshkov, A.I., Manceau, A., 2002. Structure of
878 heavy metal sorbed birnessite. Part 2. Results from electron diffraction. *Am. Mineral.* **87**,
879 1646-1661.
- 880 Dymond, J., Lyle, B., Finney, B., Piper, D.Z., Murphy, K., Conard, R., Pisias, N., 1984.
881 Ferromanganese nodules from MANOP Sites H, S, and R – control of mineralogical and
882 chemical composition by multiple accretionary processes. *Geochim. Cosmochim. Acta* **48**,
883 931-949.
- 884 Faure, G., 1998. *Principles and Applications of Geochemistry*. 2ne ed. Princeton Hall, New Jersey.
885 pp. 513.
- 886 Ford, R.G., Kemner, K.M., Bertsch, P.M., 1999. Influence of sorbate-sorbent interactions on the
887 crystallization kinetics of nickel- and lead-ferrihydrite coprecipitates. *Geochim. Cosmochim.*
888 *Acta* **63**, 39-48.
- 889 Gilmore, E.A., Evans, G.J., Ho, M.D., 2001. Radiochemical assessment of the readsorption and
890 redistribution of lead in the SM&T sequential extraction procedure. *Anal. Chim. Acta* **439**,
891 139-151.
- 892 Glasby, G.P., 2000. Manganese: predominant role of nodules and crusts. In: Schulz, H.D., Zabe,
893 M. (Eds.), *Marine Geochemistry*. Springer, Berlin, pp. 335-372.
- 894 Goldberg, E.D., 1961. Chemistry in the Oceans. In: Sears, M. (Ed.), *Oceanography*, vol. 67. Am.
895 Assoc. Adv. Sci. Publ., pp. 583-597.
- 896 Goldberg, E.D., Koide, M., Schmitt, R., Smith, R., 1963. Rare-earth distributions in the marine
897 environment. *J. Geophys. Res.* **68**, 4209-4217.
- 898 Goldberg, E.D., 1965. Minor elements in sea-water. In: Riley, J.P., Skirrow, G. (Eds.), *Chemical*
899 *Oceanography*. vol. 1. Academic Press. pp. 163-196.
- 900 Halbach, P., Segl, M., Puteanus, D., Mangini, A., 1983. Co-fluxes and growth rates in
901 ferromanganese deposits from central Pacific seamount areas. *Nature* **304**, 716-719.

- 902 Halbach, P., Friedrich, G., von Stackelberg, U., 1988. *The Manganese Nodule Belt of the Pacific*
903 *Ocean*. Enke, Stuttgart.
- 904 Haley, B.A., Klinkhammer, G.P., McManus, J., 2004. Rare earth elements in pore waters of
905 marine sediments. *Geochim. Cosmochim. Acta* **68**, 1265-1279.
- 906 Hazemann, J.L., Nayouf, K., Debergevin, F., 1995. Modelization by finite-elements of sagittal
907 focusing. *Nucl. Instr. Meth. in Phys. Res.* **B97**, 547-550.
- 908 Hem, J.D., 1978. Redox processes at surfaces of manganese oxide and their effects on aqueous
909 metal ions. *Chem Geol* **21**, 199-218.
- 910 Hochella, M.F., Kasama, T., Putnis, A., Putnis, C.V., Moore, J.N., 2005a. Environmentally
911 important, poorly crystalline Fe/Mn hydrous oxides: Ferrihydrite and a possibly new
912 vernadite-like mineral from the Clark Fork River Superfund Complex. *Am. Mineral.* **90**,
913 718-724.
- 914 Hochella, M.F., Kasama, T., Putnis, A., Putnis, C.V., Moore, J.N., 2005b. Direct observation of
915 heavy metal-mineral association from the Clark Fork River Superfund Complex: Implications
916 for metal transport and bioavailability. *Geochim. Cosmochim. Acta* **69**, 1651-1663.
- 917 Hu, Z., Bertram, S., Kaindl, G., 1994. X-ray-absorption study of PrO₂ at high pressure. *Phys. Rev.*
918 *B* **49**, 39-43.
- 919 Hudson-Edwards, K.A., 2000. Heavy metal-bearing Mn oxides in river channel and floodplain
920 sediments. In: Cotter-Howells, J.D., Campbell, L.S., Valsami-Jones, E., Batchelder, M. (Eds).
921 *Environmental Mineralogy: Microbial Interactions, Anthropogenic Influences, Contaminated*
922 *Land and Waste Management*, vol. 9. Mineralogical Society. London, pp. 207-226.
- 923 Jeon, B.-H., Dempsey, B.A., Burgos, W.D., Royer, R.A., 2003. Sorption kinetics of Fe(II), Zn(II),
924 Co(II), Ni(II), Cd(II), and Fe(II)/Mn(II) onto hematite. *Wat. Res.* **37**, 4135-4142.
- 925 Jo, T., Kotani, A., 1985. Theory of core photoabsorption spectra in CeO₂. *Solid State Commun.*
926 **54**, 451-456.
- 927 Kaindl, G., Schmiester, G., Sampathkumaran, E.V., Wachter, P., 1988. Pressure-induced changes

- 928 in L_{III} x-ray-absorption near-edge structure of CeO₂ and CeF₄: Relevance to 4f-electronic
929 structure. *Phys. Rev. B* **38**, 10174-10177.
- 930 Kawabe, I., Ohta, A., Miura, N., 1999. Distribution coefficients of REE between Fe
931 oxyhydroxide precipitates and NaCl solutions affected by REE-carbonate complexation.
932 *Geochem. J.* **33**, 181-197.
- 933 Koschinsky, A., Halbach, P., 1995. Sequential leaching of marine ferromanganese precipitates:
934 genetic implications. *Geochim. Cosmochim. Acta* **59**, 5113-5132.
- 935 Koschinsky, A., Hein, J.R., 2003. Uptake of elements from seawater by ferromanganese crusts:
936 solid-phase associations and seawater speciation. *Marine Geol.* **198**, 331-351.
- 937 Koschinsky, A., Stascheit, A., Bau, M., Halbach, P., 1997. Effects of phosphatization on the
938 geochemical and mineralogical composition of marine ferromanganese crusts. *Geochim.
939 Cosmochim. Acta* **61**, 4079-4094.
- 940 Kotani, A., Okada, K., Okada, M., 1987. Theory of 3d-XPS and L₃-XAS in CeF₄. *Solid State
941 Commun.* **64**, 1479-1482.
- 942 Kuhn, T., Bau, M., Blum, N., Halbach, P., 1998. Origin of negative Ce anomalies in mixed
943 hydrothermal-hydrogenetic Fe-Mn crusts from the Central Indian Ridge. *Earth Planet Sci.
944 Lett.* **163**, 207-220.
- 945 Kuhn, T., Bostick, B.C., Koschinsky, A., Halbach, P., Fendorf, S., 2003. Enrichment of Mo in
946 hydrothermal Mn precipitates: Possible Mo sources, formation process and phase
947 associations. *Chem. Geol.* **199**, 29-43.
- 948 Langmuir, D., 1997. *Aqueous Environmental Geochemistry*. Prentice-Hall, New Jersey, 350 pp.
- 949 Lanson, B., Drits, V.A., Gaillot, A.C., Silvester, E., Plançon, A., Manceau, A., 2002a. Structure of
950 heavy metal sorbed birnessite. Part I. Results from X-ray diffraction. *Am. Mineral.* **87**,
951 1631-1645.
- 952 Lanson, B., Drits V.A., Feng, Q., Manceau, A., 2002b. Crystal structure determination of
953 synthetic Na-rich birnessite: Evidence for a triclinic one-layer cell. *Am. Mineral.* **87**,

- 954 1662-1671.
- 955 Latrille, C., Elsass, F., van Oort, F., Denaix, L., 2001. Physical speciation of trace metals in
956 Fe-Mn concretions from a rendzic lithosol developed on Sinemurian limestones (France).
957 *Geoderma* **100**, 127-146.
- 958 Leciejewicz, J., 1961. On the crystal structure of tetragonal (red) PbO. *Acta Cryst.* **14**,
959 1304-1305.
- 960 Liu, F., Colombo, C., Adamo, P., He, J.Z., Violante, A., 2002. Trace elements in manganese-iron
961 nodules from a Chinese Alfisol. *Soil Sci. Soc. Am. J.* **66**, 661-670.
- 962 Manceau, A., Llorca, S., Calas, G., 1987. Crystal chemistry of cobalt and nickel in lithiophorite
963 and asbolane from New Caledonia. *Geochim. Cosmochim. Acta* **51**, 105-113.
- 964 Manceau, A., Charlet, L., 1992. X-ray absorption spectroscopic study of the sorption
965 of Cr(III) at the oxide/water interface. I Molecular mechanism of Cr(III)
966 oxidation on Mn oxides. *J. Coll. Interf. Sci.* **148**, 443-458.
- 967 Manceau, A., Gorshkov, A.I., Drits, V.A., 1992a. Structural chemistry of Mn, Fe, Co, and Ni in
968 manganese hydrous oxides: Part I. Information from XANES spectroscopy. *Am. Mineral.* **77**,
969 1133-1143.
- 970 Manceau, A., Charlet, L., Boisset, M.C., Didier, B., Spadini, L., 1992b. Sorption and speciation
971 of heavy metals on Fe and Mn hydrous oxides. From microscopic to macroscopic. *Appl. Clay*
972 *Sci.* **7**, 201-223.
- 973 Manceau, A., Boisset, M.C., Sarret, G., Hazemann, J.L., Mench, M., Cambier, P., Prost, R., 1996.
974 Direct determination of lead speciation in contaminated soils by EXAFS spectroscopy.
975 *Environ. Sci. Technol.* **30**, 1540-1552.
- 976 Manceau, A., Drits, V.A., Silverster, E., Bartoli, C, Lanson, B., 1997. Structural mechanism of
977 Co^{2+} oxidation by the phylломanganate buserite. *Am. Mineral.* **82**, 1150-1175.
- 978 Manceau, A., Chateigner, D., Gates, W.P., 1998. Polarized EXAFS, distance-valence
979 least-squares modeling (DVLS) and quantitative texture analysis approaches to the structural

- 980 refinement of Garfield nontronite. *Phys. Chem. Mineral.* **25**, 347-365.
- 981 Manceau, A., Lanson, B., Drits, V.A., Hazemann, J.L., Gorshkov, A., Chaillout-Bougerol, C.,
982 1999. Sorption mechanism of Zn, Cu, and Pb on birnessite by X-ray and electron diffraction,
983 and powder and polarized EXAFS spectroscopy. EUG10, March 28-April 1, *Journal of*
984 *Conference Abstracts* **4**, 666.
- 985 Manceau, A., Lanson, B., Drits, V.A., 2002a. Structure of heavy metal sorbed birnessite. Part III.
986 Results from powder and polarized extended X-ray absorption fine structure spectroscopy.
987 *Geochim. Cosmochim. Acta* **66**, 2639-2663.
- 988 Manceau, A., Marcus, M.A., Tamura, N., 2002b. Quantitative speciation of heavy metals in soils
989 and sediments by synchrotron X-ray techniques. *Rev. Mineral. Geochem.* **49**, 341-428.
- 990 Manceau, A., Tamura, N., Celestre, R.S., MacDowell, A.A., Geoffroy, N., Sposito, G., Padmore,
991 H.A., 2003. Molecular-scale speciation of Zn and Ni in soil ferromanganese nodules from
992 loess soils of the Mississippi basin. *Environ. Sci. Technol.* **37**, 75-80.
- 993 Manceau, A., Tommaseo, C., Rihs, S., Geoffroy, N., Chateigner, D., Schlegel, M., Tisserand, D.,
994 Marcus, M.A., Tamura, N., Chen, Z.S., 2005. Natural speciation of Mn, Ni and Zn at the
995 micrometer scale in a clayey paddy soil using X-ray fluorescence, absorption, and diffraction.
996 *Geochim. Cosmochim. Acta* **69**, 4007-4034.
- 997 Manceau, A., Lanson, M., Geoffroy, N., 2006. Natural speciation of Ni, Zn, Ba and As in
998 ferromanganese coatings on quartz using X-ray fluorescence, absorption, and diffraction.
999 *Geochimica et Cosmochimica Acta*, in press.
- 1000 Mannheim, F.T. Lane-Bostwick, C.M., 1988. Cobalt in ferromanganese crusts as a monitor of
1001 hydrothermal discharge on the Pacific seafloor. *Nature* **335**, 59-62.
- 1002 Marcus, M.A., Manceau, A., Kersten, M., 2004a. Mn, Fe, Zn and As speciation in a fast-growing
1003 ferromanganese marine nodule. *Geochim. Cosmochim. Acta* **68**, 3125-3136.
- 1004 Marcus, M., MacDowell, A.A., Celestre, R., Manceau, A., Miller, T., Padmore, H.A., Sublett,
1005 R.E., 2004b. Beamline 10.3.2 at ALS: a hard X-ray microprobe for environmental and

- 1006 materials sciences. *J. Synchrotron Rad.* **11**, 239–247.
- 1007 Martin, J.H., Gordon, R.M., Fitzwater, S., Broenkow, W.W., 1989. VERTEX: Phytoplankton /
1008 iron studies in the Gulf of Alaska. *Deep-Sea Res.* **36**, 649-680.
- 1009 Matocha, C.J., Elzinga, E.J., Sparks, D.L., 2001. Reactivity of Pb(II) at the Mn(III,IV)
1010 (oxyhydr)oxide-water interface. *Environ. Sci. Technol.* **35**, 2967-2972.
- 1011 McKenzie, R.M., 1989. Manganese oxides and hydroxides. In: Dixon, J. B., Weed, S.B. (Eds.),
1012 *Minerals in Soil Environments*. Soil Science Society of America book series, vol. 1, Soil
1013 Science Society of America, Madison, pp. 439-465.
- 1014 McLennan, S.M., 1989. Rare earth elements in sedimentary rocks: influence of provenance and
1015 sedimentary processes. *Rev. Mineral.* **21**, 169– 200.
- 1016 Moffett, J. W., Ho, J., 1996. Oxidation of cobalt and manganese in seawater via a common
1017 microbially catalyzed pathway. *Geochim. Cosmochim. Acta* **60**, 3415-3424.
- 1018 Moorby, S.A., Cronan, D.S., 1981. The distribution of elements between co-existing phases in
1019 some marine ferromanganese-oxide deposits. *Geochim. Cosmochim. Acta* **45**, 1855-1877.
- 1020 Morin, G., Ostergren, J.D., Juillot, F., Ildefonse, P., Calas, G., Brown, G.E.Jr., 1999. XAFS
1021 determination of the chemical form of lead in smelter-contaminated soils and mine tailings:
1022 Importance of adsorption processes. *Am. Mineral.* **84**, 420-434.
- 1023 Morin, G., Juillot, F., Ildefonse, P., Calas, G., Samama, J.C., Chevallier, P., Brown, G.E. Jr., 2001.
1024 Mineralogy of lead in a soil developed on a Pb-mineralized sandstone (Largentière, France).
1025 *Am. Mineral.* **86**, 92-104.
- 1026 Murray, J.W., 1974. The surface chemistry of hydrous manganese dioxide. *J. Colloid Interface*
1027 *Sci.* **46**, 357-371.
- 1028 Murray, J.W. Dillard, J.G., 1979. The oxidation of cobalt(II) adsorbed on manganese dioxide.
1029 *Geochim. Cosmochim. Acta* **43**, 781-787.
- 1030 Nishimura, M., 1983. *Marien Chemistry*, Sangyo Tosho, Tokyo, pp. 82-83 (in Japanese).
- 1031 Nomura, M. Koyama, A., 1996. Design and performance of a new XAFS beamline at the photon

- 1032 factory; BL-12C. *KEK Report* **95-15**.
- 1033 Nomura, M., 1998. Dead-time correction of a multi-element SSD for fluorescent XAFS. *J.*
1034 *Synchrotron Rad.* **5**, 851-853.
- 1035 Ohta, A., Ishii, S., Sakakibara, M., Mizxuno, A., Kawabe, I., 1999. Systematic correlation of the
1036 Ce anomaly with the Co/(Ni+Cu) ratio and Y fractionation from Ho in distinct types of
1037 Pacific deep-sea nodules. *Geochem. J.* **33**, 399-417.
- 1038 Piepgras, D.J., Jacobsen, S.B., 1992. The behavior of rare earth elements in seawater: Precise
1039 determination of variations in the North Pacific water column. *Geochim. Cosmochim. Acta*
1040 **56**, 1851-1862.
- 1041 Piper, D.Z., 1974. Rare earth elements in ferromanganese nodules and other marine phases.
1042 *Geochim. Cosmochim. Acta* **38**, 1007-1022.
- 1043 Pozas, R., Rojas, T.C., Ocana, M., Serna, C.J., 2004. The nature of Co in synthetic
1044 Co-substituted goethites. *Clays Clay Mineral.* **52**, 760-766.
- 1045 Proux, O., Nassif, V., Prat, A., Ulrich, O., Lahera, E., Biquard, X., Menthonnex, J.J., Hazemann,
1046 J.L., 2006. Feedback system of a liquid-nitrogen-cooled double-crystal monochromator:
1047 design and performances. *J. Synch. Rad.* **13**, 59-68.
- 1048 Rao, K.J., Wong, J., 1984. A XANES investigation of the bonding of divalent lead in solids. *J.*
1049 *Chem. Phys.* **81**, 4832-4843.
- 1050 Rendell, P.S., Batley, G.E., Cameron, A.J., 1980. Adsorption as a control of metal concentrations
1051 in sediment extracts. *Environ. Sci. Tehnol.* **14**, 314-318.
- 1052 Ressler, J., 1998. WinXAS: a program for x-ray absorption spectroscopy data analysis under
1053 MS-Windows. *J. Synchrotron Rad.* **5**, 118-122.
- 1054 Rouse, R.C., 1971. The crystal structure of quenselite. *Zeit. Krist.* **134**, 321-332.
- 1055 Schaule, B.K., Patterson, C.C., 1981. Lead concentrations in the northeast Pacific: Evidence for
1056 global anthropogenic perturbations. *Earth Planet. Sci. Lett.* **54**, 97-116.
- 1057 Scheinost, A.C., Abend, S., Pandya, K.I., Sparks, D.L., 2001. Kinetic controls on Cu and Pb

- 1058 sorption by ferrihydrite. *Environ. Sci. Technol.*, **35**, 1090-1096.
- 1059 Schlegel, M.L., Manceau, A., Charlet, L., Chateigner, D., Hazemann, J.L., 2001. Sorption of
1060 metal ions on clay minerals. III. Nucleation and epitaxial growth of Zn phyllosilicate on the
1061 edges of hectorite. *Geochim. Cosmochim. Acta* **65**, 4155-4170.
- 1062 Schwertmann, U. Cornell, R.M., 2000. *Iron oxides in the laboratory*, Wiley-VCH. Weinheim, pp.
1063 67-112.
- 1064 Sholkovitz, E.R., 1989. Artifacts associated with the chemical leaching of sediments for
1065 rare-earth elements. *Chem. Geol.* **77**, 47-51.
- 1066 Silvester, E., Manceau, A., Drits, V.A., 1997. The structure of synthetic monoclinic Na-rich
1067 birnessite and hexagonal birnessite. Part 2. Results from chemical studies and EXAFS
1068 spectroscopy. *Am. Mineral.* **82**, 962-978.
- 1069 Smedley, P.L., Kinniburgh, D.G., 2002. A review of the source, behaviour and distribution of
1070 arsenic in natural waters. *Applied Geochem.* **17**, 517-568.
- 1071 Soldatov, A.V., Ivanchenko, T.S., Longa, S.D., Kotani, A., Iwamoto, Y., Bianconi, A., 1994.
1072 Crystal-structure effects in the Ce L₃-edge x-ray absorption spectrum of CeO₂:
1073 Multiple-scattering resonances and many-body final states. *Phys. Rev. B* **50**, 5074-5080.
- 1074 Sorem, R.K., Fewkes, R.H., 1977. Internal Characteristics. In: Glasby, G.P. (Ed.), *Marine*
1075 *Manganese Deposits*, Elsevier, Amsterdam, pp. 147-183.
- 1076 Spadini, L., Manceau, A., Schindler, P.W., Charlet, L., 1994. Structure and stability of Cd²⁺
1077 surface complexes on ferric oxides. I. Results from EXAFS spectroscopy. *J. Coll. Interf. Sci.*
1078 **168**, 73-86.
- 1079 Spadini, L., Schindler, P.W., Charlet, L., Manceau, A., Ragnarsdottir, K.V., 2003. Hydrous ferric
1080 oxide: evaluation of Cd-HFO surface complexation models combining Cd_K EXAFS data,
1081 potentiometric titration results, and surface site structures identified from mineralogical
1082 knowledge. *J. Coll. Interf. Sci.* **266**, 1-18.
- 1083 Stumm, W., 1993. *Chemistry of the solid-water interface*. John Wiley & Sons.

- 1084 Sumaoka, J., Igawa, T., Furuki, K., Komiyama, M., 2000. Homogeneous Ce(IV) Complexes for
1085 Efficient Hydrolysis of Plasmid DNA. *Chem. Lett.* **29**, 56-57.
- 1086 Szytula, A., Burewicz, A., Dimitrijevic, Z., Krasnicki, S., Rzany, H., Todorovic, J., Wanic, A.,
1087 Wolski, W., 1968. Neutron Diffraction Studies of α -FeOOH. *Phys. Stat. Sol.* **26**, 429-434.
- 1088 Takahashi, Y., Minai, Y., Ambe, H., Makide, Y., Ambe, F., Tominaga, T., 1997. Simultaneous
1089 determination of stability constants of humate complexes with various metal ions using
1090 multitracer technique. *Sci. Total Environ.* **198**, 61–71.
- 1091 Takahashi, Y., Minai, Y., Ambe, H., Makide, Y., Ambe, F., 1999. Comparison of adsorption
1092 behavior of multiple inorganic ions on kaolinite and silica in the presence of humic acid
1093 using the multitracer technique. *Geochim. Cosmochim. Acta* **63**, 815–836.
- 1094 Takahashi, Y., Shimizu, H., Usui, A., Kagi, H., Nomura, M., 2000. Direct observation of
1095 tetravalent cerium in ferromanganese nodules and crusts by X-ray absorption near-edge
1096 structure (XANES). *Geochim. Cosmochim. Acta* **64**, 2929-2935.
- 1097 Takahashi, Y., Sakami, H., Nomura, M., 2002a. Determination of the oxidation state of cerium in
1098 rocks by Ce L_{III}-edge X-ray absorption near-edge structure. *Anal. Chim. Acta* **468**, 345-354.
- 1099 Takahashi, Y., Usui, A., Okumura, K., Uruga, T., Nomura, M., Murakami, M., Shimizu, H., 2002.
1100 Application of XANES for the determination of oxidation states of Co and Pb in natural
1101 ferromanganese nodules. *Chem. Lett.* **31**, 366-367.
- 1102 Takematsu, N., Sato, Y., Okabe, S., 1989. Factors controlling the chemical composition of
1103 marine manganese nodules and crusts: a review and synthesis. *Mar. Chem.* **26**, 41-56.
- 1104 Takematsu, N., 1998. *Manganese nodule*. Koseisha Kouseikaku, Tokyo (in Japanese).
- 1105 Teo, B.K., 1986. EXAFS: basic principles and data analysis. Springer-Verlag.
- 1106 Terashima, S., Usui, A., Imai, N., 1995. 2 new GSJ geochemical reference samples - syenite
1107 JSy-1 and manganese-nodule JMn-1. *Geostandards Newslett.* **19**, 221-229.
- 1108 Toner, B., Manceau, A., Webb, S.M., Sposito, G., 2006. Zinc sorption to biogenic
1109 hexagonal-birnessite particles within a hydrated bacterial biofilm. *Geochim. Cosmochim.*

- 1110 *Acta* **70**, 27-43.
- 1111 Trivedi, P., Dyer, J.A., Sparks, D.L., 2003. Lead sorption onto ferrihydrite. 1. A macroscopic and
1112 spectroscopic assessment. *Environ. Sci. Technol.* **37**, 908-914.
- 1113 Uruga, T., Tanida, H., Yoneda, Y., Takeshita, K., Emura, S., Takahashi, M., Harada, M., Nishihata,
1114 Y., Kubozono, Y., Tanaka, T., Yamamoto, T., Maeda, H., Kamishima, O., Takabayashi, Y.,
1115 Nakata, Y., Kimura, H., Goto, S., Ishikawa, T., 1999. The XAFS beamline BL01B1 at
1116 SPring-8. *J. Synchrotron Rad.* **6**, 143-145.
- 1117 Usui, A., Bau, M., Yamazaki, T., 1997. Manganese microchimneys buried in the Central Pacific
1118 pelagic sediments: evidence of intraplate water circulation? *Mar. Geol.* **141**, 269-285.
- 1119 Villalobos, M., Toner, B., Bargar, J., Sposito, G., 2003. Characterization of the manganese oxide
1120 produced by *Pseudomonas putida* strain MnB1. *Geochim. Cosmochim. Acta* **67**, 2649-2662.
- 1121 Villalobos, M., Bargar, J., Sposito, G., 2005. Mechanisms of Pb(II) sorption on a biogenic
1122 manganese oxide. *Environ. Sci. Technol.* **39**, 569-576.
- 1123 Villalobos M., Lanson B., Manceau A., Toner B., Sposito G., 2006. Structural model for the
1124 biogenic Mn oxide produced by *Pseudomonas putida*. *Am. Mineral.* **91**, 489-502.
- 1125 Vodyanitskii, Y.N., Sivtsov, A.V., 2004. Formation of ferrihydrite, ferroxhyte, and vernadite in
1126 soil. *Eurasian Soil Sci.* **37**, 863-875.
- 1127 Wehrli, B., 1990. Redox reactions of metal ions at mineral surfaces. In: Stumm, W. (Ed.), *Aquatic*
1128 *Chemical Kinetics*, Wiley, New York, pp. 311-336.
- 1129 Wen, X., De Carlo, E.H., Li, Y.H., 1997. Interelement relationships in ferromanganese crusts
1130 from the central Pacific ocean: Their implications for crust genesis. *Mar. Geol.* **136**, 277-297.
- 1131

FIGURE CAPTIONS

- 1132
- 1133
- 1134 Fig. 1. Co (a) and Pb (b) abundances as a function of the Mn/Fe ratio for the series of
1135 ferromanganese oxides studied here and by Usui et al. (1997). Concentrations are from bulk
1136 and average EPMA analyses
- 1137 Fig. 2. REE patterns for the three genetic-type ferromanganese oxides. (a) Data normalized to
1138 PAAS; (b) Data normalized to the average REE abundances in deep seawater (Piepgras and
1139 Jacobsen, 1992).
- 1140 Fig. 3. Results from sequential dissolution of D535, AD14, D1-X1, and D21-m3 (hydrogenetic),
1141 and FG352 and G181 (diagenetic) ferromanganese oxides. Metal speciation has been
1142 operationally defined by Koschinsky and Halbach (1995) and Koschinsky and Hein (2003)
1143 as follows. Fraction 1: exchangeable cations and Ca carbonate fraction; Fraction 2: Mn oxide
1144 fraction; Fraction 3: Fe oxyhydroxide fraction; Fraction 4: residual fraction, mainly
1145 consisting of silicates and aluminosilicates.
- 1146 Fig. 4. Co, Ce, and Pb abundances against Mn/Fe ratio in CD25, D535, and AD14. Data from
1147 electron microprobe analyses. Numbers in parenthesis are correlation coefficients (r^2).
- 1148 Fig. 5. Cerium L_{III}-edge XANES spectra of a selection of ferromanganese oxides and references.
1149 Ce-sorption reaction times are one hour on δ -MnO₂ and HFO-1 and 120 hours on HFO-2.
1150 An overlay plot of the CeCl₃ spectrum is represented in dotted line for comparison. In some
1151 spectra, the position of the maximum of the 1st derivative is indicated by an arrow. CeO₂ and
1152 Ce(OH)₄ have a shoulder at 5727 eV pointed out by an asterisk.
- 1153 Fig. 6. Cerium L_{III}-edge micro XANES spectra at spot 1 in the growth structure and at spot 2 in
1154 the Fe-rich area of CD25. The locations of the analyzed spots are indicated by a cross in the
1155 X-ray fluorescence maps.
- 1156 Fig. 7. Cobalt K-edge XANES spectra of a selection of ferromanganese oxides and references.
- 1157 Fig. 8. Cobalt K-edge micro XANES spectra at spots 1 and 2 on the X-ray fluorescence map

1158 presented in Figure 7. The difference spectrum suggests that 10-15 % of Co is divalent at
1159 spot 2.

1160 Fig. 9. (a) Lead L_{III}-edge XANES spectra of hydrogenetic and diagenetic ferromanganese oxides
1161 and reference compounds. (b) First derivative of some XANES spectra.

1162 Fig. 10. Pb L₃-edge EXAFS spectra of untreated (D1-X1, AD14 and D21-m3) and
1163 hydroxylamine-treated (D1-X1-Fe, AD14-Fe and D21-m3-Fe) hydrogenetic ferromanganese
1164 oxides (a-e). The D21-m3 spectrum was best simulated (Sum-sq = 0.039) with a mixture of
1165 AD14 and D21-m3-Fe, in proportions of 50 and 47 %, respectively. Precision: 10 % of total
1166 Pb (f).

1167 Fig. 11. Pb L₃-edge EXAFS spectra (a,c) and Fourier transforms (b,d) of hydroxylamine-treated
1168 D21-m3 (D21-m3-Fe) and untreated AD14 compared to Pb-sorbed ferrihydrite (PbHFO100,
1169 pH 6.5) and Pb-sorbed δ -MnO₂ (Pbd112, pH 5) references. The numbers after the code
1170 names are the Pb to sorbent metal (Fe or Mn) mole ratio in parts per thousand.

1171 Fig. 12. Model fits of the Pb-EXAFS data for lead sorbed on ferrihydrite (PbHFO), δ -MnO₂
1172 (PbdBi) and well-crystallized birnessite (PbBi). The data are in dashed lines, and the models
1173 in solid lines, and the best-fit parameters for each model are listed in Table 5. The
1174 contributions from the Pb-O, Pb-Fe (ferrihydrite), and Pb-Mn (δ -MnO₂ and birnessite)
1175 nearest shells have been filtered by Fourier transformation.

1176 Fig. 13. Pb L₃-edge EXAFS spectra (a) and Fourier transforms (b) of Pb sorbed on δ -MnO₂
1177 (PbdBi series) and well-crystallized birnessite (PbBi) at different Pb/Mn ratio.

1178 Fig. 14. Structural model for the uptake mechanism of Pb on Mn³⁺-free phyllomanganate. TCS
1179 and DES are triple-corner and double-edge sharing complexes. At low surface loading, Pb
1180 occupies both lateral (DES) and basal (TCS) sites of the MnO₂ layer. On the lateral site, the
1181 base of the Pb pyramid is formed by two conjoined edges from two neighboring Mn(IV)
1182 octahedra (tridendate edge-sharing complex). On the basal site, the base of the Pb pyramid is
1183 formed by the face of a vacant Mn(IV) layer octahedron and, therefore, is parallel to the

1184 layer plane (tridendate corner-sharing complex).

1185 Fig. 15. Electronic waves from the two Mn shells at $R = 3.46$ ($N = 1.0$, $\sigma^2 = 0.014 \text{ \AA}^2$) and $R =$
1186 3.70 \AA ($N = 3.0$, $\sigma^2 = 0.014 \text{ \AA}^2$) for PbBi31 in the model fit of Pb-sorbed phyllosulfate
1187 proposed by Villalobos et al. (2005). The two waves are out-of-phase at 6.5 \AA^{-1} ($\Delta E_0 = 0$
1188 eV).

Electronic Annex captions

1189
1190
1191 **Fig. EA-1.** X-ray diffraction patterns of hydrogenetic samples. F = feldspar (mostly albite), FeOx
1192 = poorly crystallized Fe oxyhydroxide, Gt = goethite, P = phyllosilicate, Ph = phillipsite, Qtz =
1193 quartz. The 7 Å and 10 Å phyllomanganates are one-water (7 Å) and two-water (10 Å) layer
1194 hydrates of vernadite. Hydrogenetic Mn oxides have low Mn/Fe ratios (Table 2) and weak basal
1195 reflections. Recording conditions for all patterns: Cu K α radiation, angular range = 5 - 80 °2 θ ,
1196 step size = 0.04 °2 θ , counting time = 40 s/pt.

1197
1198 **Fig. EA-2.** X-ray diffraction patterns of diagenetic samples. Diagenetic and hydrothermal Mn
1199 oxides (Fig. EA-3) have high Mn/Fe ratios and intense basal reflections.

1200
1201 **Fig. EA-3.** X-ray diffraction patterns of hydrothermal and mixed hydrogenetic-hydrothermal
1202 samples. C = calcite, H = halite, T = todorokite.

1203

Table 1. List of the samples of ferromanganese oxides studied in this work.

Sample name	Sampling site			Cruise name	Type of deposition	Mineralogy of Mn oxides ^a
	Latitude	Longitude	Depth (m)			
D535	13°00.6'S	159°17.6'W	5222	Hakurei-maru GH83-3	HG	Fe-vernadite
CD25	16°26.0'N	169°32.3'W	2320	Farnella FN-86-HW	HG	Fe-vernadite
AD14	14°11.8'N	167°24.4'E	1617	Hakurei-maru 96S	HG	Fe-vernadite
D1-X1	32°04.5'N	138°31.5'E	2600	Moana Wave MW9503	HG	Fe-vernadite
D21-m3	31°23.5'N	138°45.3'E	1110	Moana Wave MW9503	HG	Fe-vernadite
D465, inner	09°03.4'N	174°04.1'W	5968	Hakurei-maru GH80-5	HG	Fe-vernadite
D465, outer	09°03.4'N	174°04.1'W	5968	Hakurei-maru GH80-5	DG	10Å-vernadite
D513	01°05.2'S	166°10.0'W	5341	Hakurei-maru GH82-4	DG	10Å-vernadite
D514	00°45.9'S	166°07.0'W	5200	Hakurei-maru GH82-4	DG	10Å-vernadite
FG352	03°15.8'N	169°41.1'W	5370	Hakurei-maru GH81-4	DG	10Å-vernadite
G181	07°01.4'N	171°59.7'W	5660	Hakurei-maru GH76-1	DG	10Å-vernadite
B6	30°17.8'N	172°10.5'W	5350	Hakurei-maru GH80-1	DG	10Å-vernadite
F243-1	07°40.2'N	172°56.3'W	5907	Hakurei-maru GH80-1	DG	10Å-vernadite
D11-X9	32°00.1'N	139°10.1'E	1575	Moana Wave MW9503	HT	10Å+7Å-vernadite + todorokite
D12-X2	31°58.0'N	139°04.2'E	1590	Moana Wave MW9503	HT	Hexagonal birnessite
D21-103	31°23.5'N	138°45.3'E	1110	Moana Wave MW9503	HT	10Å+7Å-vernadite +ctodorokite
31GTV2-3	25°24.0'S	69°45.4'E	2800	SO92 Sonne	HG + HT	Fe-vernadite
31GTV6-11	25°24.0'S	69°45.4'E	2800	SO92 Sonne	HG + HT	Fe-vernadite

^a Turbostratic (i.e., *c*-disordered) phyllomanganates found in marine ferromanganese oxides have been named δ -MnO₂, buserite and birnessite in the literature on the basis of the intensity and position of basal reflections by XRD. Today, it appears that there is no fundamental structural difference between all these phyllomanganate varieties. As discussed in Manceau et al. (2006), the use of the generic term vernadite, which dates back to long before the three others (Betekhtin, 1940), is preferred to describe natural turbostratic phyllomanganates. In sample D12-X2, the phyllomanganate layers are stacked regularly with an hexagonal sequence as in synthetic HBi

(Silvester et al., 1997). Diffraction patterns are presented in Electronic Annex.

Table 2. Bulk chemical analyses.

	Mn	Fe	Mn/Fe	Co	Cu	Ni	Zn	Pb
	(wt.%)		(wt. ratio)			(mg/kg)		
D535	12.8	12.7	1.01	4750	1020	2820	465	714
CD25	13.1	12.1	1.08	6350	513	1690	741	1170
AD14	13.4	11.7	1.15	8370	904	3450	1420	1640
D1-X1	5.57	17.1	0.326	830	276	870	441	1650
D21-m3	14.4	13.9	1.04	2450	177	1460	401	1870
G181	29.4	4.68	6.28	1630	11500	8550	1340	162
B6	25.6	5.30	4.83	1140	18800	14300	1310	234
F243-1	26.8	4.20	6.38	1540	12800	10900	1680	211
D513	24.9	5.99	4.16	717	18200	14400	1330	182
D514	20.8	9.30	2.24	1750	9650	10400	908	448
FG352	25.9	6.07	4.27	1320	19200	13300	1170	259
D11-X9	41.6	0.420	99.0	d.l.	13.4	61.0	73.0	35.0
D12-X2	44.2	0.080	553	46.0	4.6	119	54.5	56.0
D21-103	43.2	d.l.	-	176	62.5	295	26.0	34.0
31GTV2-3 ^a	12.4	17.2	0.721	755	563	1200	518	408
31GTV6-11 ^a	15.4	19.8	0.778	966	713	1730	541	315

^aData from Kuhn et al. (1998).

d.l.: below detection limit.

Table 3. Electron microprobe analyses (wt.%) in main growth structures.

Sample name	Mn	Fe	Mn/Fe	Al	Si	P	Ti	Co	Ce	Pb	N (number of analyzed points); observed minor phase
D535	20.5-34.4 27.9 (3.6)	10.4-22.2 16.4 (3.1)	0.92-3.29 1.81 (0.64)	0.353-2.10 0.69 (0.42)	0.244-2.61 0.645 (0.674)	0.109-0.266 0.217 (0.045)	0.713-1.15 0.904 (0.123)	0.228-1.33 0.679 (0.428)	0.134-0.294 0.208 (0.041)	0.001-0.169 0.087 (0.044)	N=30; Opal with high Fe content.
CD25	15.5-36.3 26.0 (4.5)	9.35-27.8 16.5 (4.5)	0.570-3.82 1.75 (0.67)	0.044-0.654 0.244 (0.147)	0.167-4.40 0.919 (1.13)	0.150-0.379 0.248 (0.055)	0.829-2.88 1.44 (0.45)	0.243-1.32 0.648 (0.352)	0.028-0.825 0.167 (0.093)	d.l.-0.393 0.154 (0.104)	N=90; Opal with high Fe content and particle with high contents of Fe and Ti.
AD14	19.1-39.4 29.5 (6.2)	6.47-30.2 16.7 (8.5)	0.635-5.81 2.64 (1.86)	0.073-0.422 0.151 (0.057)	0.043-0.816 0.268 (0.193)	0.211-1.88 0.561 (0.430)	0.412-1.20 0.735 (0.251)	0.168-2.32 0.867 (0.758)	0.076-0.260 0.152 (0.046)	0.137-0.392 0.263 (0.071)	N=60; Phosphate and Fe precipitate (Mn/Fe is around 0.07).
D465, inner	18.9-38.2 28.6 (4.9)	2.27-15.5 9.45 (3.28)	1.27-16.3 3.96 (3.37)	0.822-3.96 2.47 (0.734)	0.135-2.03 0.566 (0.352)	0.047-0.270 0.141 (0.050)	0.210-1.07 0.705 (0.258)	0.060-0.404 0.260 (0.077)	d.l.-0.138 0.077 (0.039)	0.019-0.126 0.058 (0.025)	N=30
D465, outer	16.1-39.7 25.4 (8.1)	0.173-18.5 8.54 (6.19)	0.955-217 26.4 (51.0)	0.755-4.01 2.33 (0.70)	0.021-1.30 0.633 (0.358)	0.017-0.264 0.135 (0.084)	d.l.-0.837 0.415 (0.289)	0.001-0.350 0.191 (0.095)	d.l.-0.129 0.059 (0.039)	d.l.-0.113 0.046 (0.036)	N=30

D514	23.3-42.8	1.47-3.30	9.14-27.6	0.604-2.24	0.461-1.82	0.036-0.072	0.067-0.749	0.092-0.308	0.111-0.182	n.m.	N=7
	36.3	2.49	15.9	1.54	1.09	0.059	0.265	0.175	0.140		
	(7.1)	(0.60)	(6.59)	(0.66)	(0.50)	(0.013)	(0.289)	(0.095)	(0.027)		
FG352	21.4-46.3	0.103-8.20	3.72-447	0.124-3.38	0.041-3.60	0.021-0.162	0.007-0.453	0.050-0.207	0.052-0.204	n.m.	N=7
	35.8	3.34	100	1.46	1.23	0.076	0.148	0.136	0.119		
	(9.1)	(2.87)	(177)	(1.07)	(1.26)	(0.051)	(0.166)	(0.057)	(0.055)		

First row = range of concentrations, second row = average values, third row (in parentheses) = standard deviations of the measured values. In some cases, the standard deviation exceeds the average value due to chemical heterogeneity. d.l.: below detection limit; n.m.: not measured.

Table 4. Bulk REE abundances (mg/kg)

Sample name	Y	La	Ce	Pr	Nd	Sm	Eu	Gd	Tb	Dy	Ho	Er	Tm	Yb	Lu	(Ce/Ce*) _{SN} ^d
D535 ^a	130	177	1230	41.3	164	38.3	8.97	40.3	5.90	33.8	6.89	20.2	2.88	19.3	2.95	3.31
CD25 ^a	188	303	844	70.8	283	62.2	15.1	64.9	9.43	58.0	11.5	32.1	4.39	27.3	4.16	1.33
AD14 ^a	131	167	573	28.4	124	25.9	6.58	30.2	4.57	29.2	6.63	20.4	2.90	18.9	3.01	1.91
D1-X1	59.6	203	1130	41.1	168	35.1	8.69	31.8	4.89	23.5	3.94	10.5	1.41	9.23	1.39	2.85
D21-m3	207	304	621	60.3	260	56.5	13.9	61.6	9.68	54.5	10.7	30.3	4.15	25.5	3.90	1.05
D465, inner	115	150	916	33.3	139	30.2	7.38	31.9	5.07	31.0	5.73	18.2	2.59	17.7	2.74	2.98
D465, outer	59.0	63.0	178	18.4	76.7	19.4	4.80	19.2	3.32	18.1	3.41	9.67	1.44	9.51	1.34	1.20
G181	41.4	44.0	91.4	13.6	58.4	14.6	4.13	14.0	2.34	13.2	2.48	6.87	1.01	6.48	0.982	0.860
B6	81.6	68.5	81.7	18.3	79.5	18.8	5.33	19.3	3.22	18.8	3.65	10.7	1.51	9.89	1.53	0.531
F243-1	37.4	36.7	84.8	11.4	49.3	12.6	3.58	12.7	2.14	11.9	2.30	6.44	0.960	6.15	0.939	0.953
D513 ^b	64.2	64.4	114	17.2	75.0	17.4	4.21	17.6	2.88	16.5	3.19	9.86	1.31	8.52	1.29	0.790
D514	86.9	103	262	25.6	106	24.3	5.82	25.5	3.85	22.4	4.25	12.0	1.68	11.2	1.64	1.17
FG352	66.9	70.9	64.4	15.4	65.7	15.1	3.43	15.1	2.52	14.1	2.87	9.04	1.21	8.65	1.17	0.448
D11-X9	32.2	4.64	5.14	0.753	3.43	0.776	0.810	1.41	0.261	2.34	0.744	2.85	0.462	3.36	0.617	0.632
D12-X2	12.9	4.24	6.59	0.791	3.68	0.773	0.180	1.08	0.180	1.38	0.370	1.32	0.211	1.60	0.269	0.827
D21-103	1.80	0.661	0.213	0.0839	0.454	0.0590	0.0207	0.103	0.0160	0.133	0.0393	0.127	0.0204	0.152	0.0259	0.208
GTV2-3 ^c	189	276	320	61.9	241	48.2	12.2	55.3	7.96	46.8	9.21	25.1	3.68	22.0	3.36	0.563
GTV6-11 ^c	186	289	253	60.9	238	48.5	12.1	54.2	7.89	46.8	9.33	25.6	3.74	22.7	3.60	0.439

^a Data from Takahashi et al. (2000) except for Y.

^b Average values of six analyses reported in Ohta et al. (1999).

^c Data from Kuhn et al. (1998).

^d (Ce/Ce*)_{SN} = the degree of Ce anomaly normalized to PAAS (McLennan, 1989).

Table 5. Pb-EXAFS for Pb sorbed phyllo-manganates and hydrous ferric oxide

Sample	Fit Model	O shell			Me ^a shell			ΔE_0 (eV)	R_p
		R (Å)	N^b	σ^2 (Å ²)	R (Å)	N^b	σ^2 (Å ²)		
PbBi31	Two-shell fit	2.30	1.6	0.011	3.72	1.3	0.008	-5	24
	Three-shell fit	2.29	1.7	0.012	3.70	1.0	0.008 ^c	-9	14
					4.09	0.8	0.008 ^c		
	Three-shell fit ^d	2.29	1.7	0.011	3.46	1 ^e	0.014	-7	24
3.70					3 ^e	0.014			
PbdBi197	Two-shell fit	2.29	2.3	0.012	3.68	0.8	0.008	-9	15
PbdBi112	Three-shell fit	2.33	2.2	0.012	3.23	0.2	0.008 ^c	-9	12
					3.73	0.6	0.008 ^c		
PbdBi44	Three-shell fit	2.33	2.3	0.012	3.23	0.3	0.008 ^c	-9	15
					3.73	0.5	0.008 ^c		
PbdBi2	Three-shell fit	2.34	2.2	0.012	3.25	0.3	0.007 ^c	-9	15
					3.76	0.5	0.007 ^c		
PbHFO100	Two-shell fit	2.36	2.8	0.013	3.39	1.6	0.014	-4	32
	Three-shell fit	2.37	2.9	0.013 ^c	3.41	1.6	0.014	-2	26
	Three-shell fit	2.36	2.9	0.013	3.26	1.9	0.014 ^c	-5	17
					3.44	2.7	0.014 ^c		
	Four-shell fit	2.38	3.3	0.014 ^c	3.32	1.9	0.014 ^c	-1	9
		2.65	1.3	0.014 ^c	3.50	2.5	0.014 ^c		

EXAFS parameters were optimized by minimizing the R_p value defined as $\text{sum}\{|k^3\chi_{exp} - k^3\chi_{fit}|\} / \text{sum}\{|k^3\chi_{exp}|\}$. The $R+\Delta$ intervals for the Fourier backtransforms were [1.1-4.2] Å for PbBi31, [1.1-3.9] Å for PbdBi197-5 and PbdBi35-7, [1.1-3.8] Å for PbdBi44-5 and PbdBi2-5, and [1.1-3.7] Å for PbHFO100.

^a Me = Mn for Mn compounds, and Me = Fe for HFO.

^b effective coordination numbers. The Pb full coordination is lost due to anharmonic structural disorder.

^c σ parameters constrained to the same value for the two sub-shells. $S_0^2 = 0.85$.

^d Same model fit as Villalobos et al. (2005)

^e Parameters fixed to the same values as in Villalobos et al. (2005)

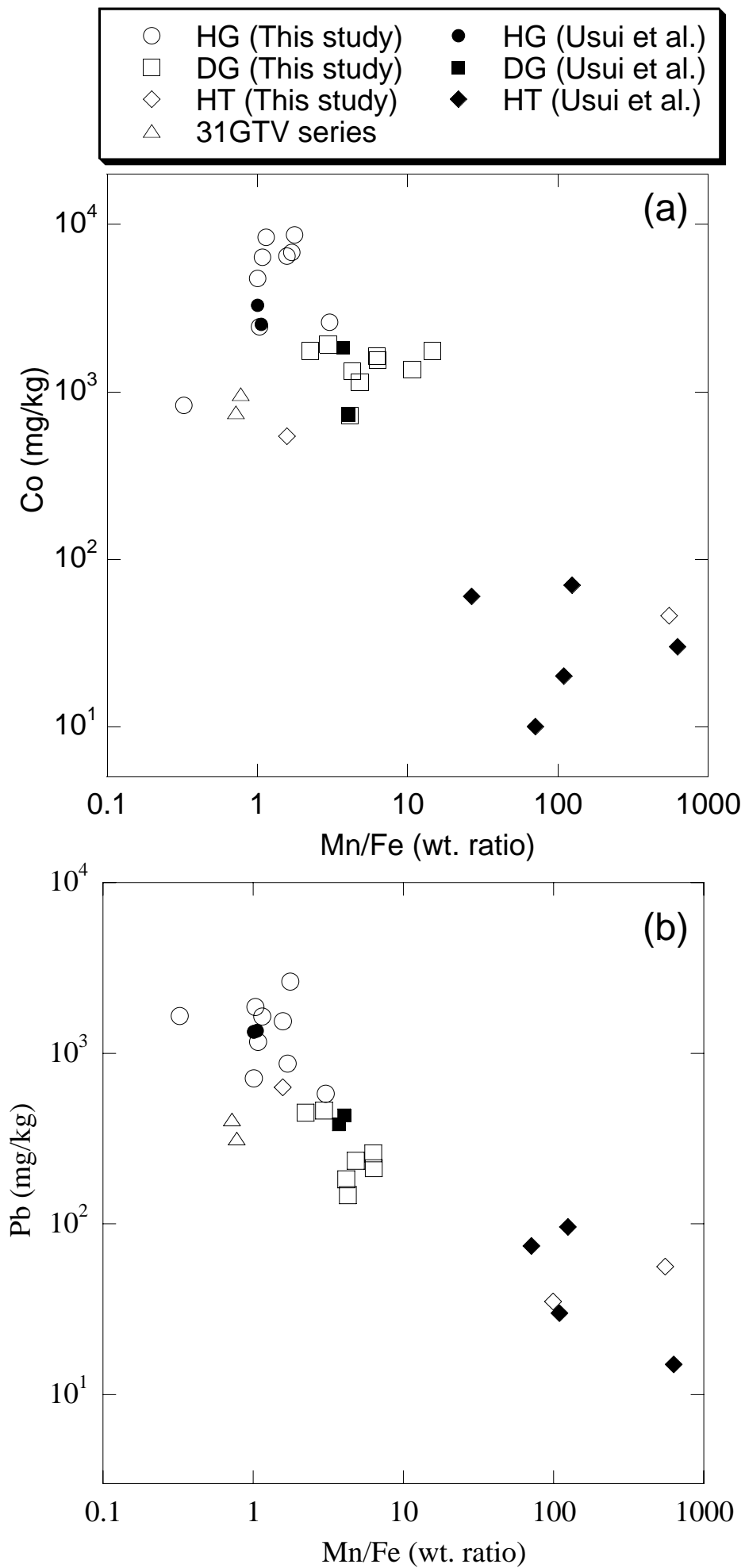


Fig.1

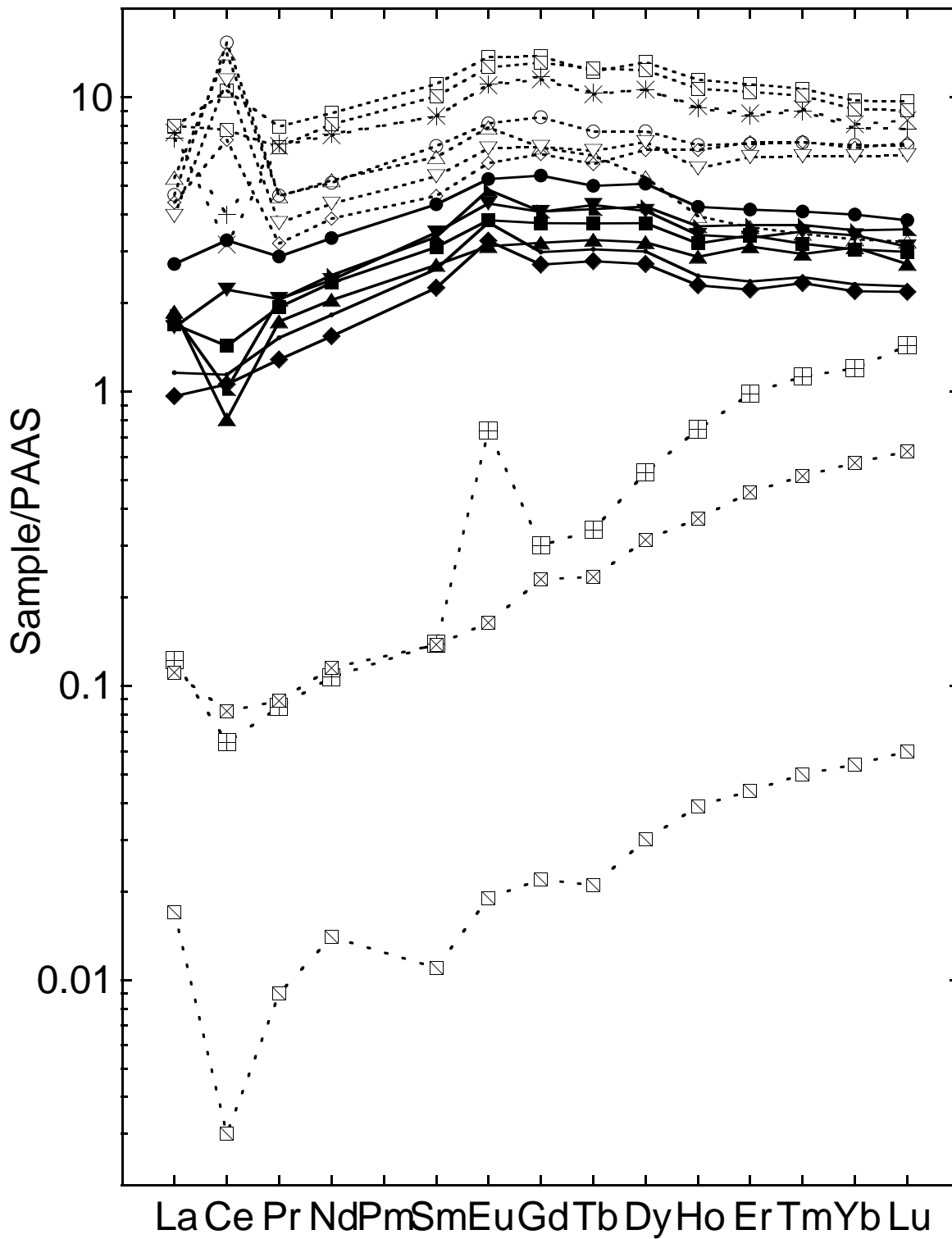
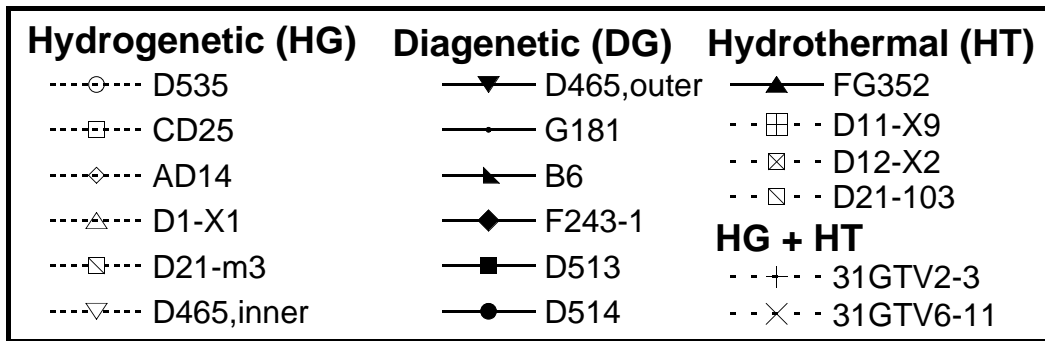


Fig.2a

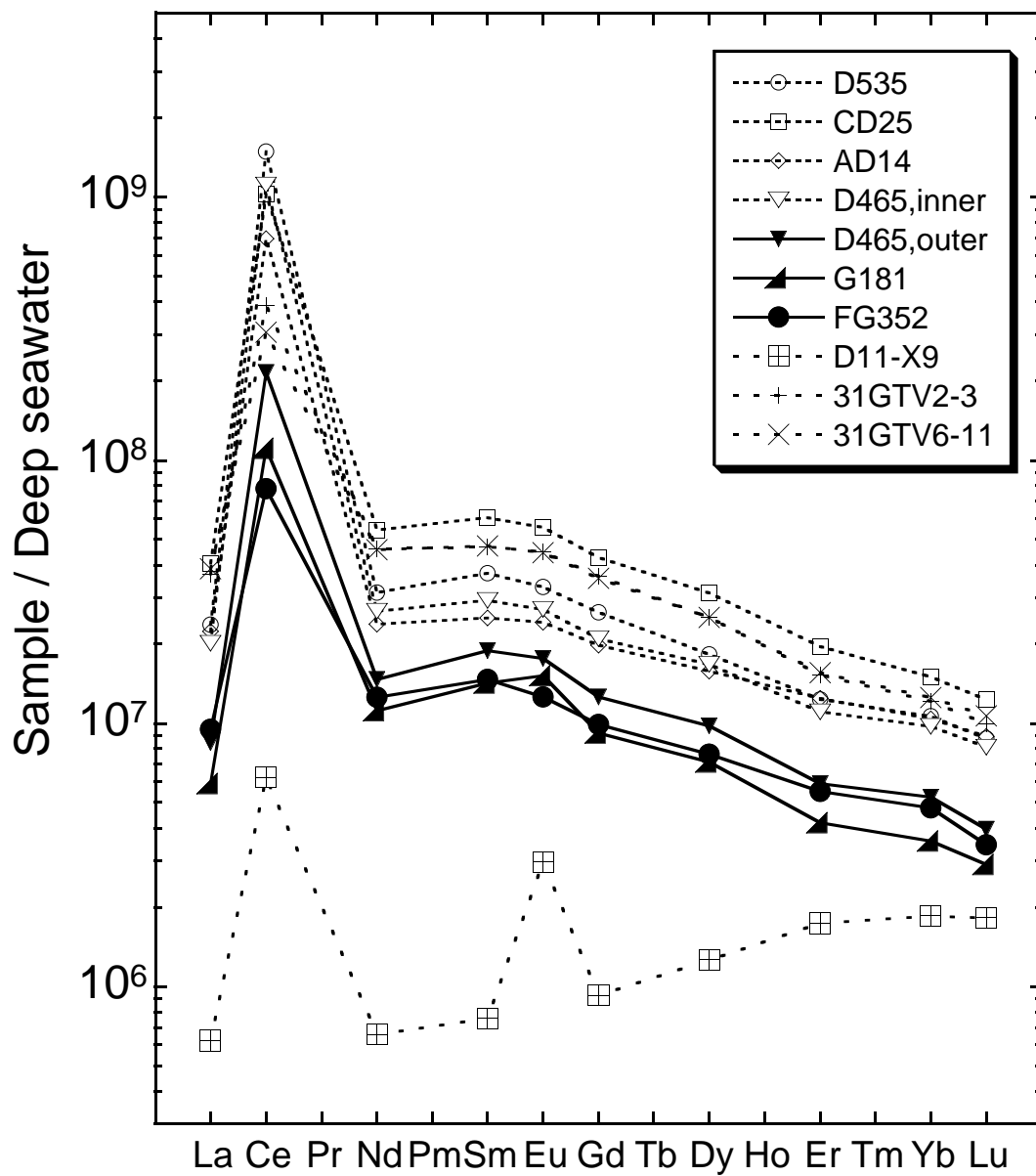


Fig.2b

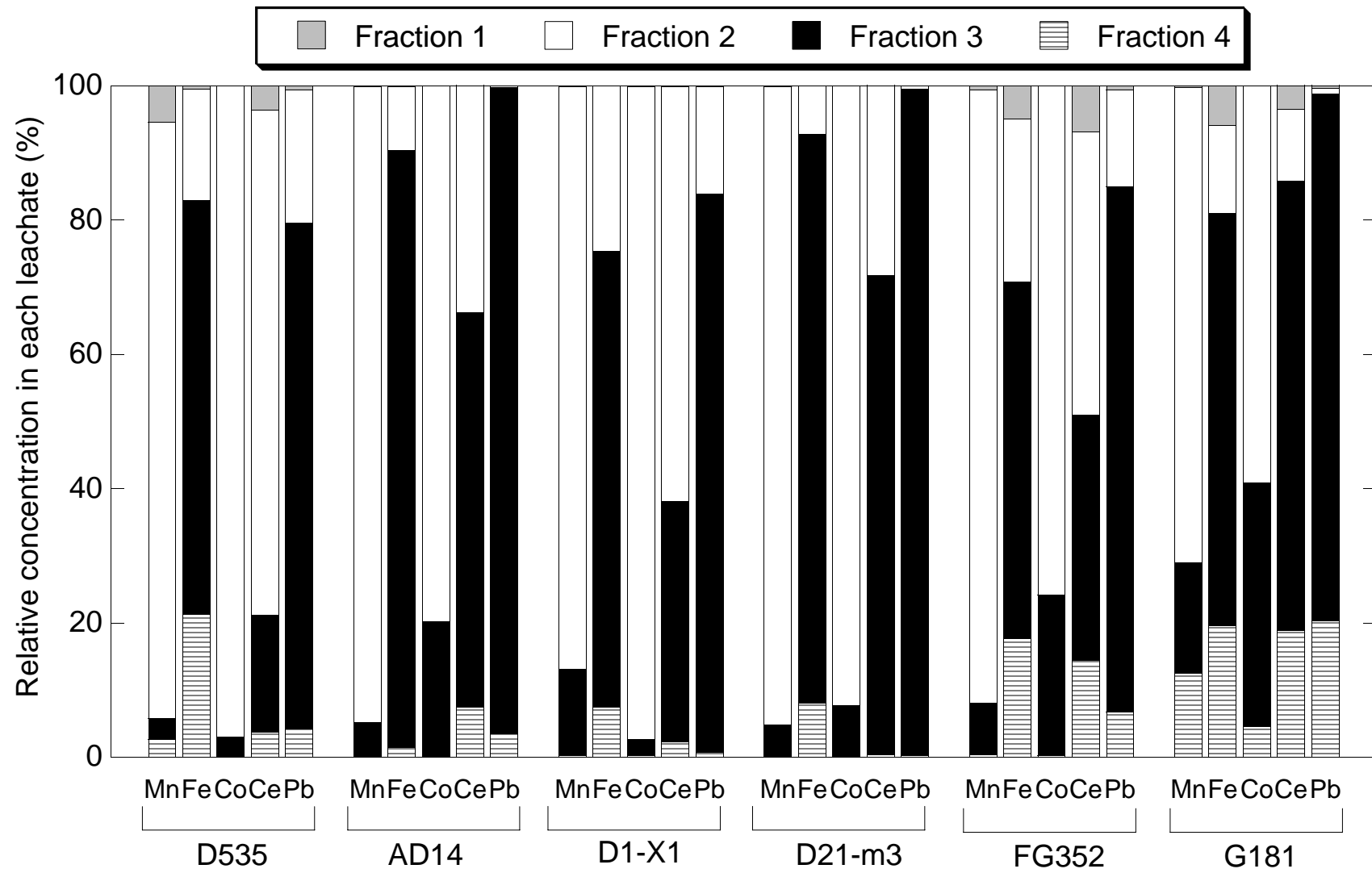


Fig.3

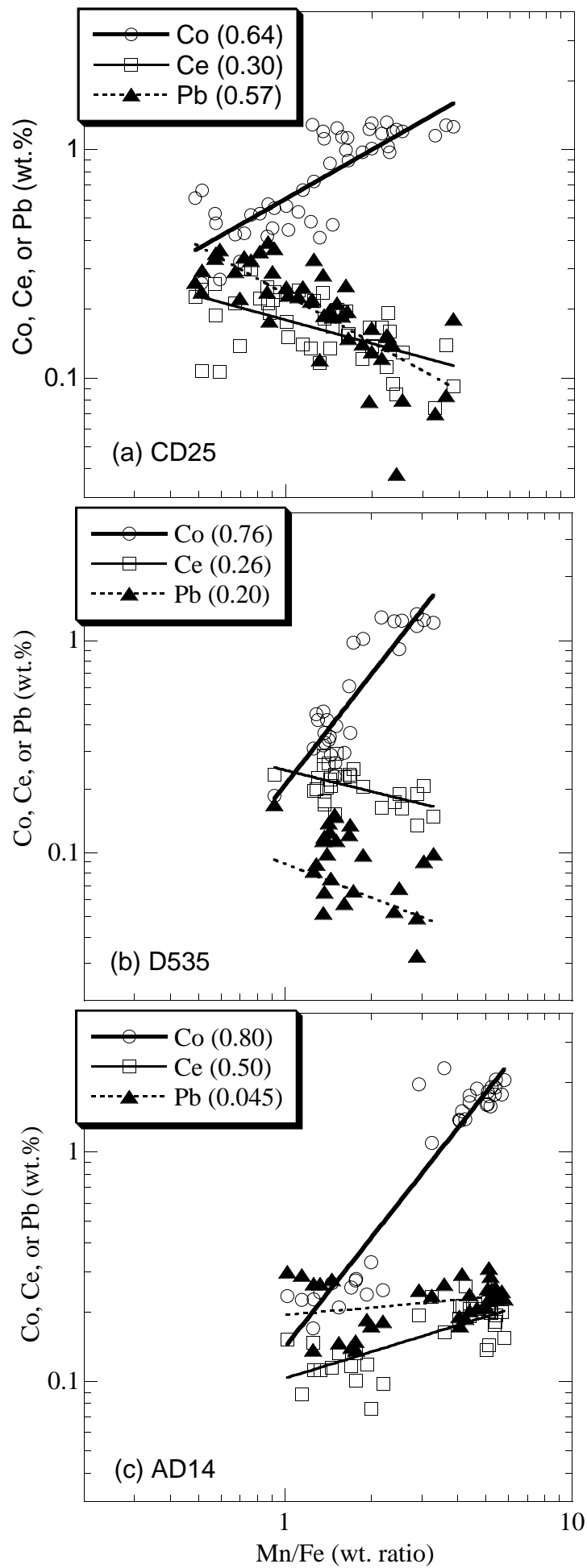


Fig. 4

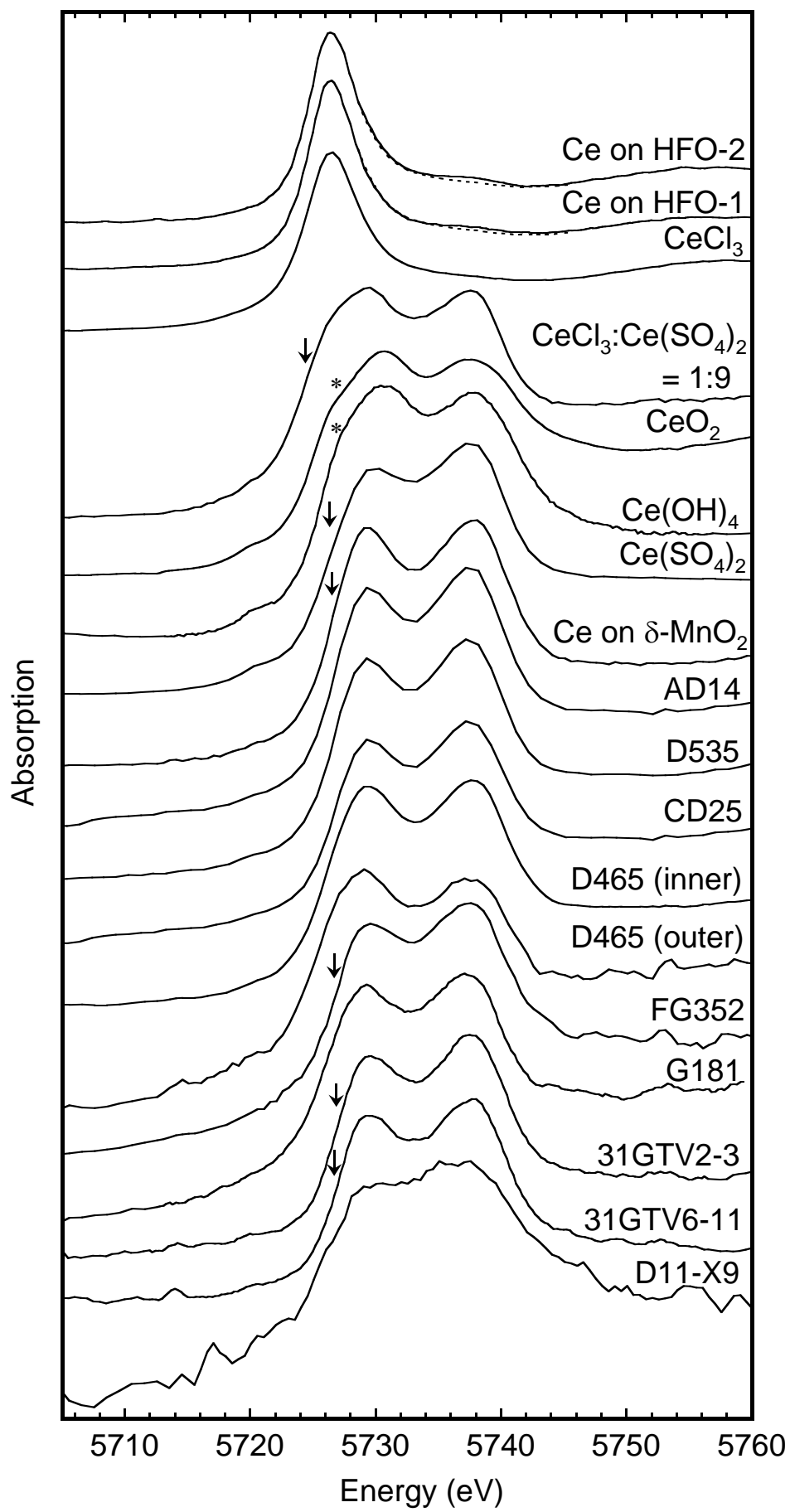


Fig.5

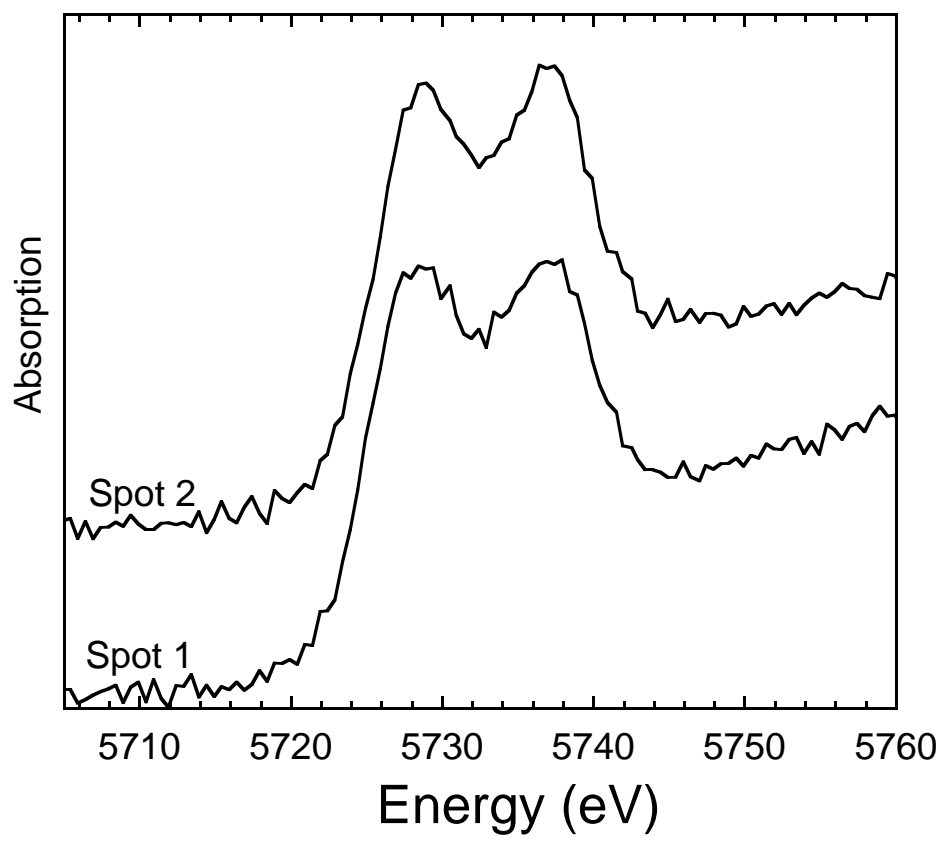
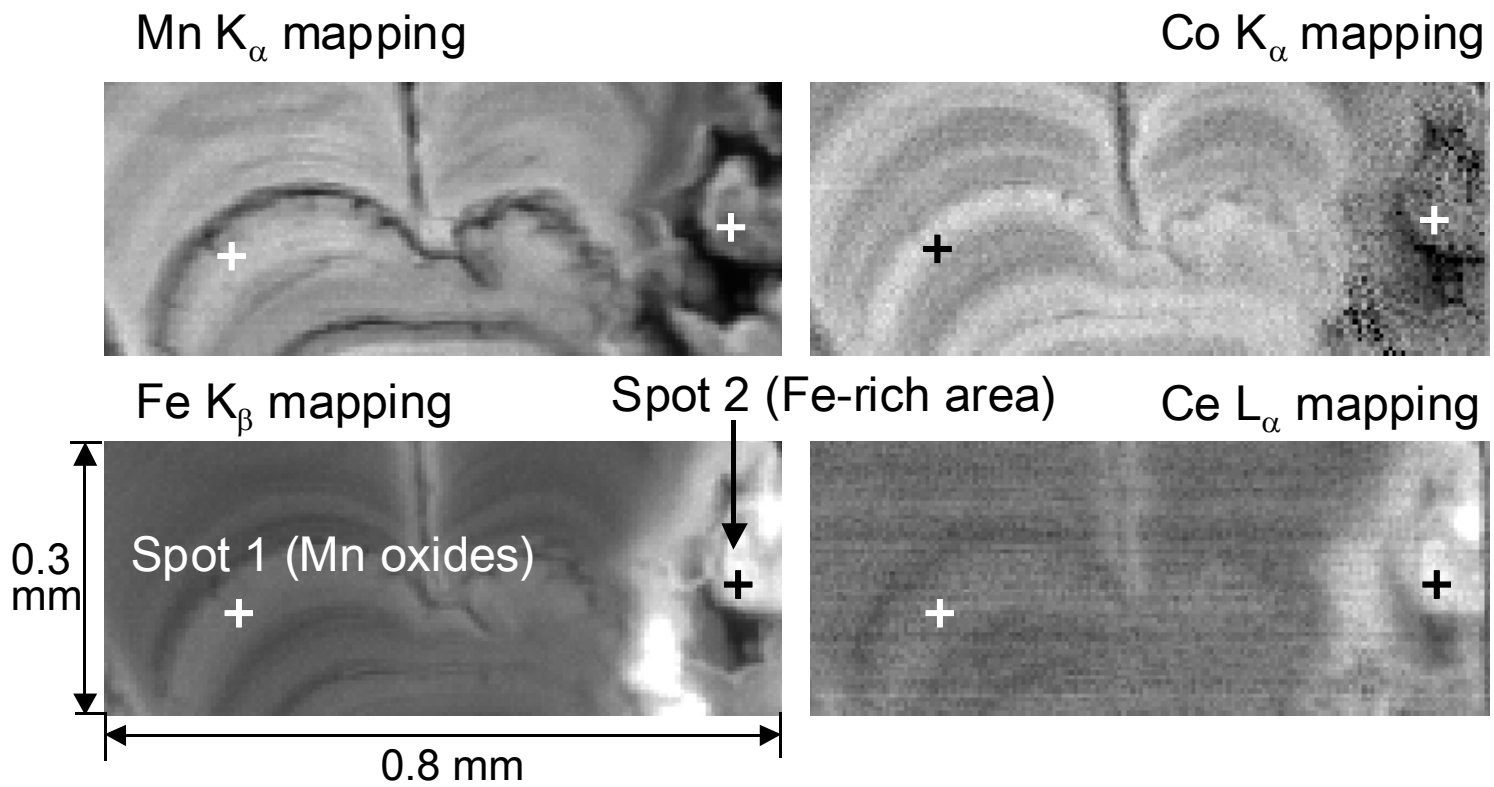


Fig.6

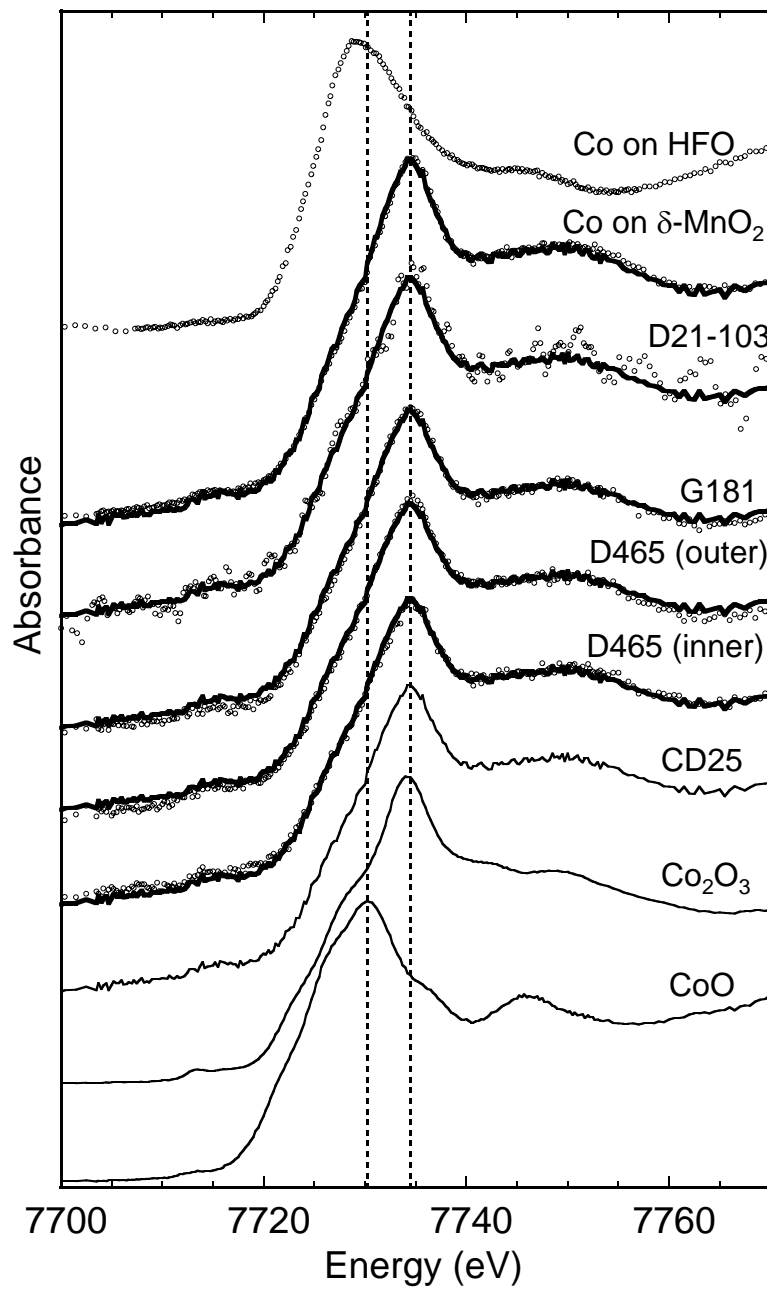


Fig.7

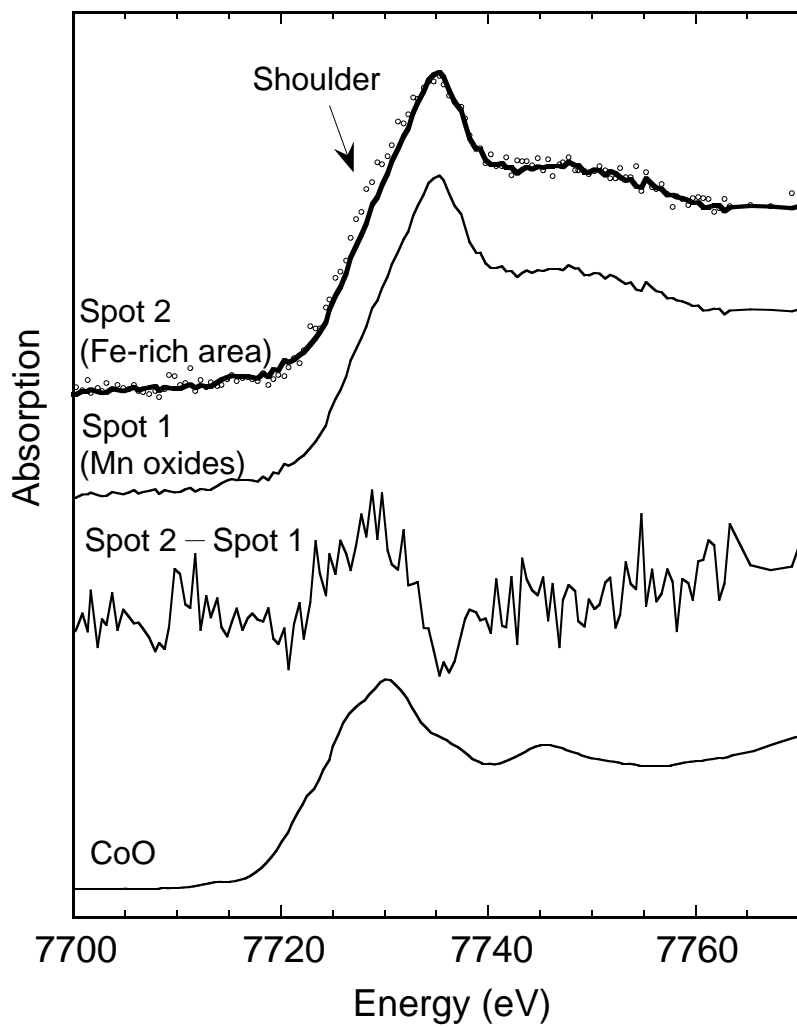


Fig.8

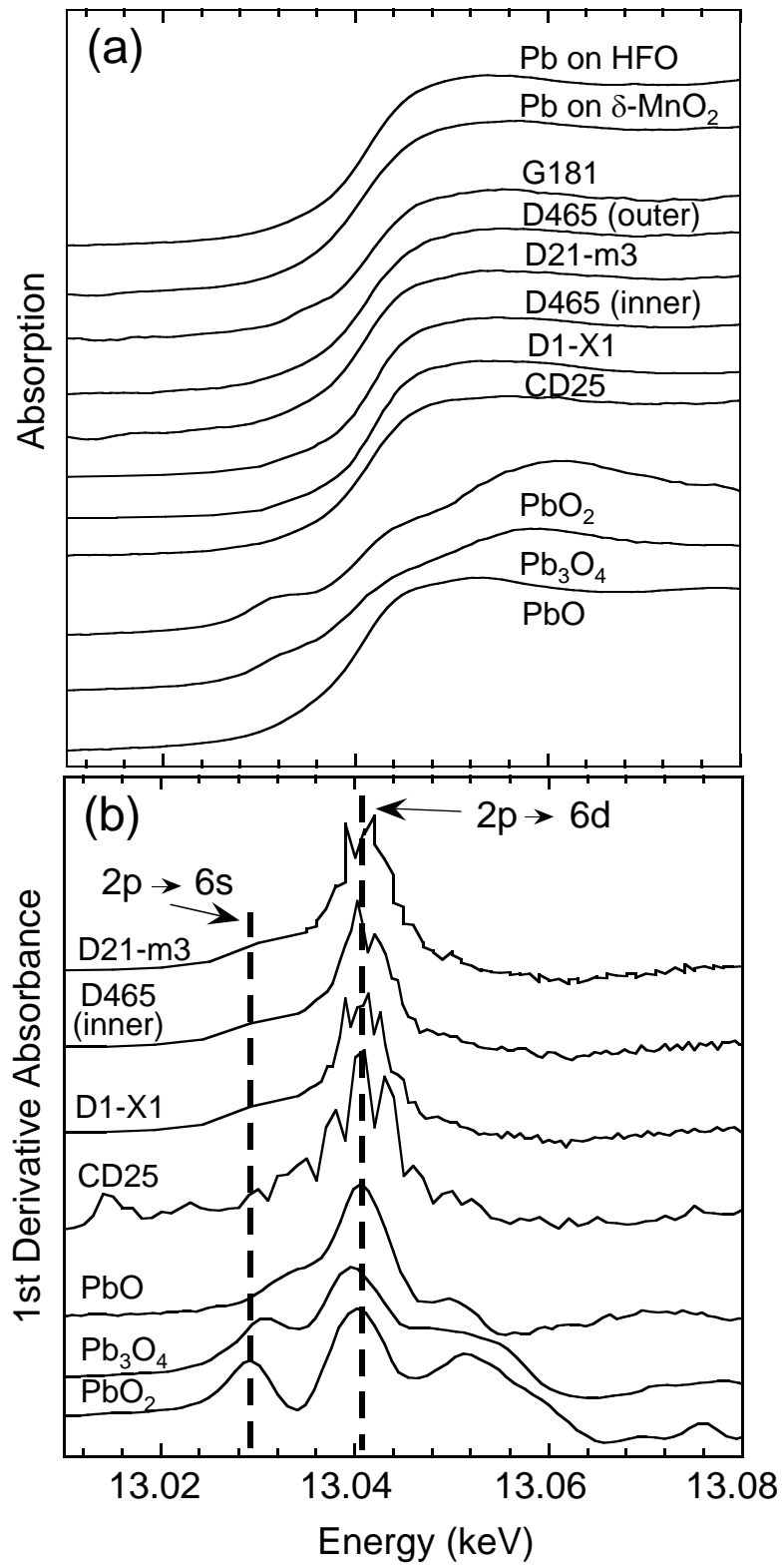


Fig.9

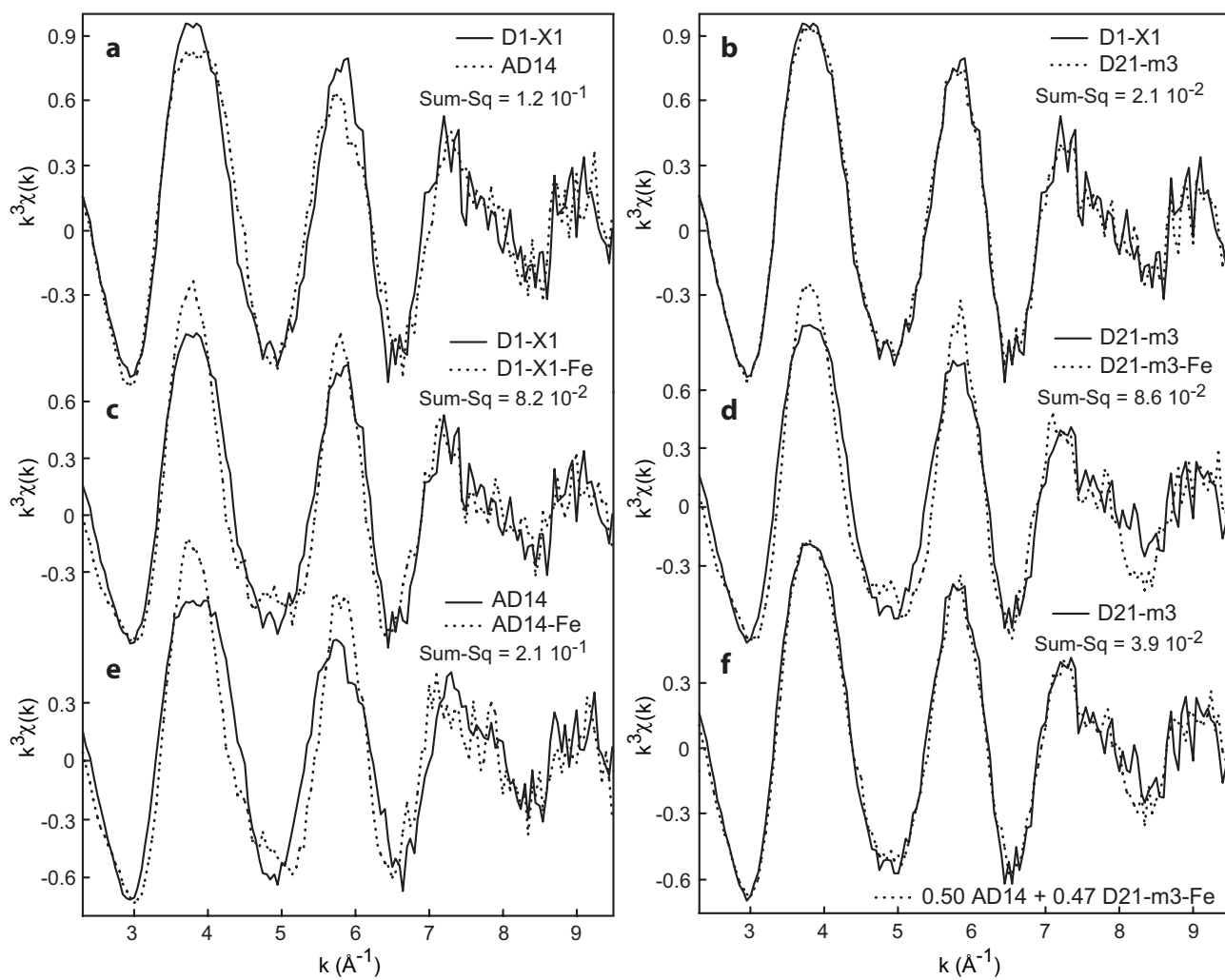


Fig. 10

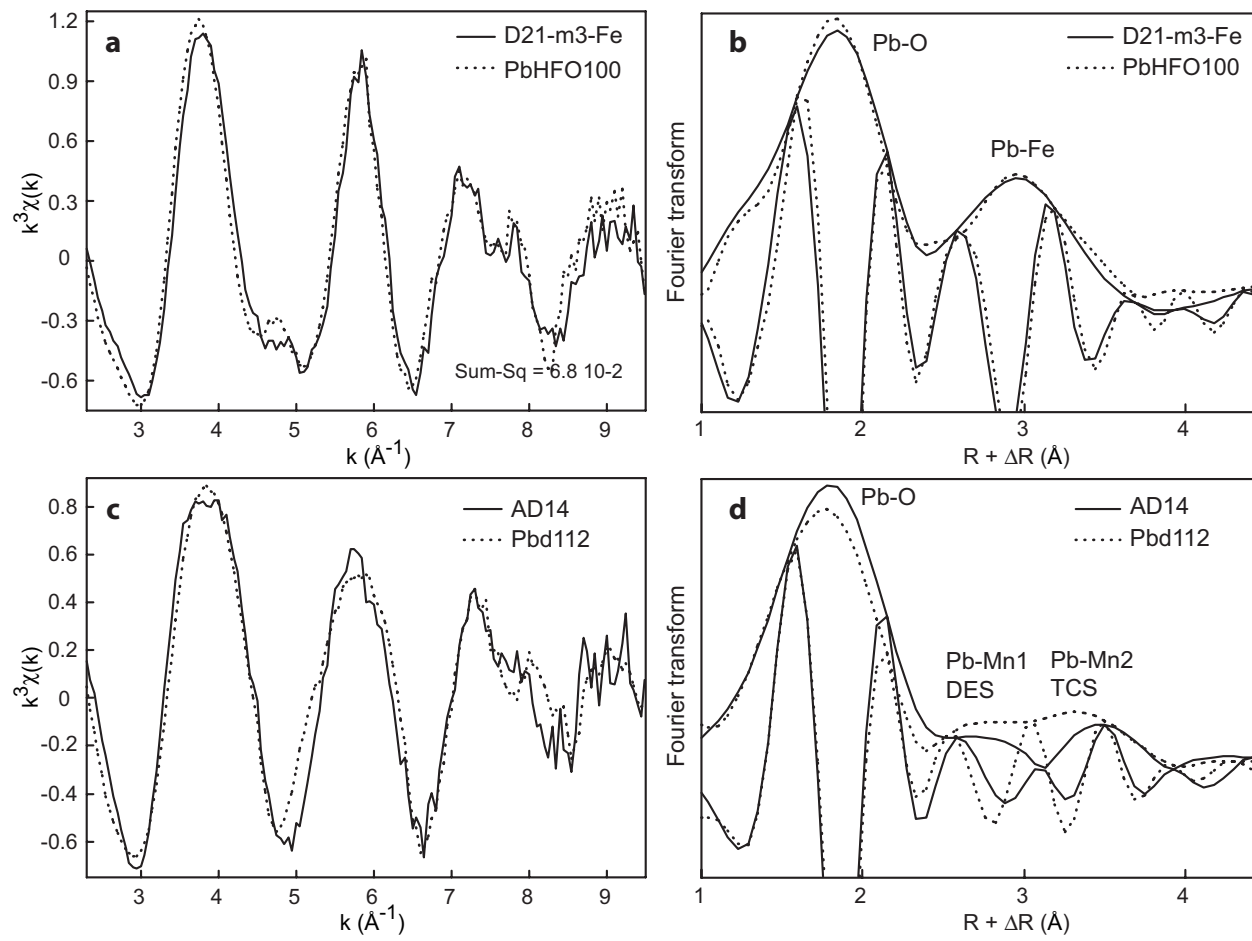


Fig. 11

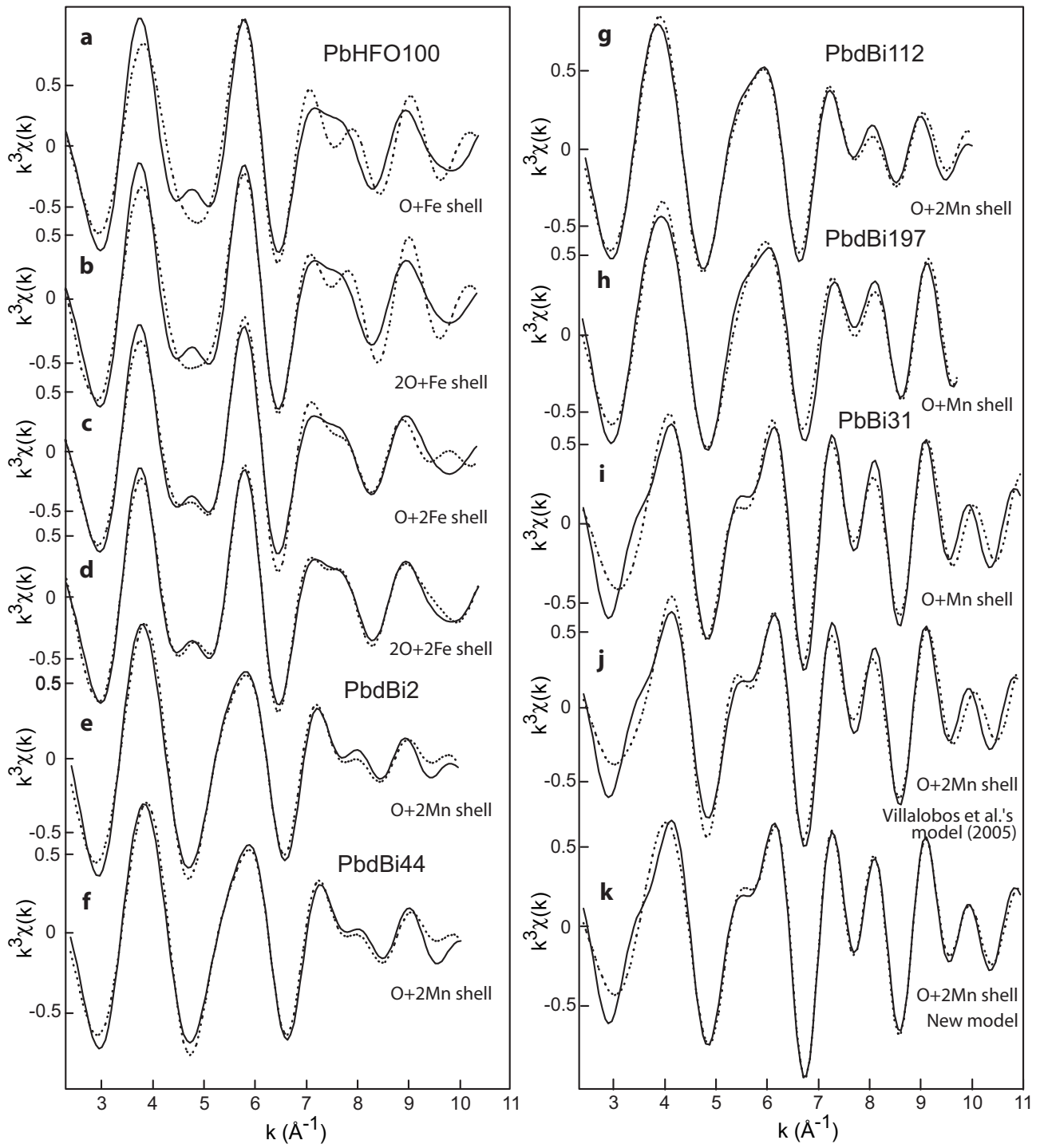


Fig. 12

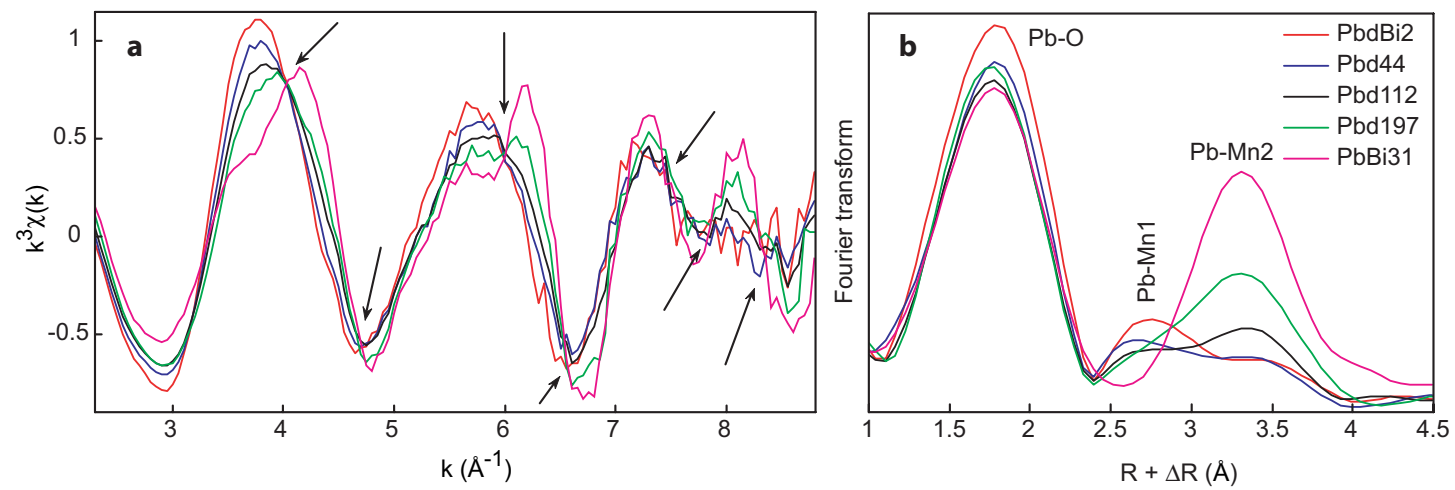


Fig. 13

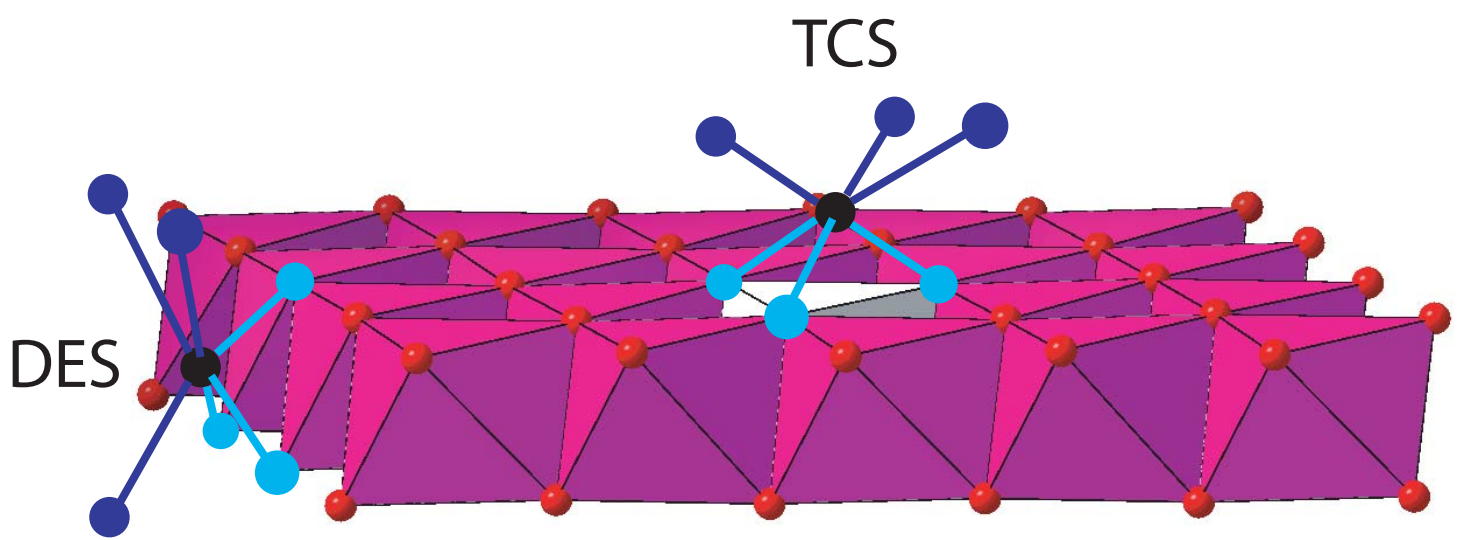


Fig. 14

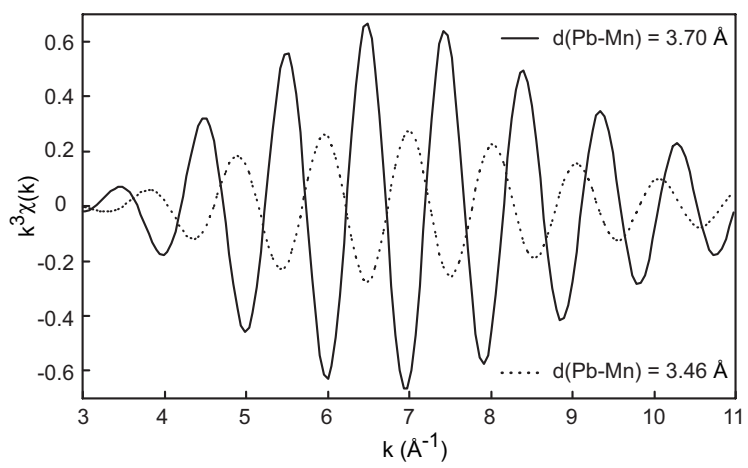


Fig. 15